POLYOXOMETALATES

Open Access
REVIEW ARTICLE

Polyoxometalate-based sub-1 nm materials: Controllable preparation and energy storage/conversion applications

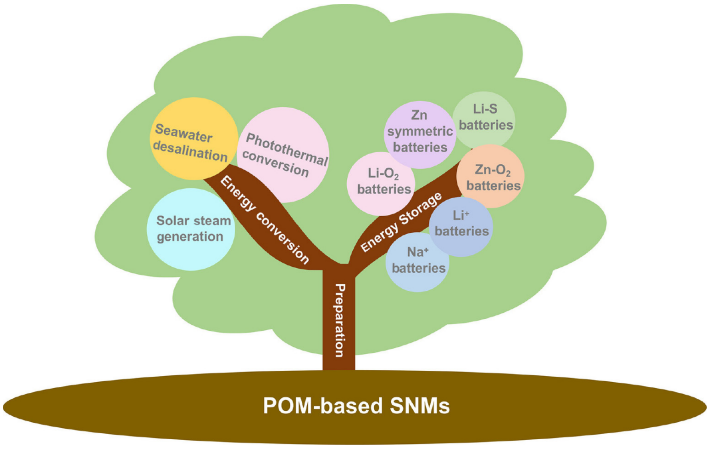
Yiting Zhang[1], Yu Zhang[1,2], and Junli Liu[1] ✉

[1] *Key Laboratory of Bio-inspired Smart Interfacial Science and Technology of Ministry of Education, School of Chemistry, Beihang University, Beijing 100191, China*
[2] *Hangzhou International Innovation Institute, Beihang University, Hangzhou 311115, China*

Cite This: *Polyoxometalates*, **2026**, *5*, 9140114

Read Online

ABSTRACT: Sub-1 nm materials (SNMs) feature large specific surface areas and near-100% atomic exposures, thus offering abundant exposed active sites and properties well suited for applications in optics, electricity, catalysis, etc. In particular, polyoxometalate (POM)-based SNMs hold great promise for energy storage/conversion applications because of their nanoscale dimensions and synergetic effect of multiple components. Despite the abundance of reported POM-based SNMs, systematic reviews of their synthesis and energy storage/conversion applications are scarce. This review summarizes progress in the synthesis of POM-based SNMs and their applications in energy storage (e.g., Li-ion, Na-ion, Li–O_2, Zn–O_2, and Li–S batteries) and conversion (e.g., photothermal conversion, solar steam generation, and seawater desalination). Moreover, we discuss the related challenges and future perspectives, providing new insights into the rational design and development of efficient POM-based SNMs suitable for energy storage and conversion.



KEYWORDS: polyoxometalates, sub-1 nm materials, energy storage, energy conversion

1 Introduction

The overexploitation of nonrenewable energy sources such as coal, oil, and natural gas has resulted in environmental pollution and a global energy crisis [1–5]. In turn, this crisis has inspired a search for new energy sources, with renewable ones (e.g., wind and solar energy) holding particular promise because of their low cost, ecofriendliness, and inexhaustibility [6–13].

Batteries rely on the interconversion of chemical and electrical energy upon charge–discharge [14–18], with notable examples including metal-ion batteries (e.g., Li-ion batteries (LIBs) [15], Na-ion batteries (SIBs) [18], and K-ion batteries) [19–22] and metal–air batteries (e.g., Li–O_2 batteries (LOBs) [23–25], Li–CO_2 batteries [26–28], Li–N_2 batteries [29–31], and Zn–O_2 batteries (ZABs) [32–34]). However, current batteries have certain limitations, e.g., insufficient capacity, sluggish reaction kinetics, and limited cycling lifetime [35–38], which hinder practical applications. The energy storage performance of batteries can be improved through the development of novel materials for battery components (e.g., electrodes, separators, and electrolytes) (Fig. 1).

The utilization of the ecofriendly and abundant solar energy is another effective way of mitigating the energy crisis [39–42]. The conversion of solar energy into thermal energy (photothermal conversion) can be used in seawater desalination [43–46], biological medicine [47–52], and catalysis [53–58]. Thus, new materials with excellent photothermal conversion properties are urgently required.

Among the numerous energy storage/conversion materials, sub-1 nm materials (SNMs), especially polyoxometalate (POM)-based

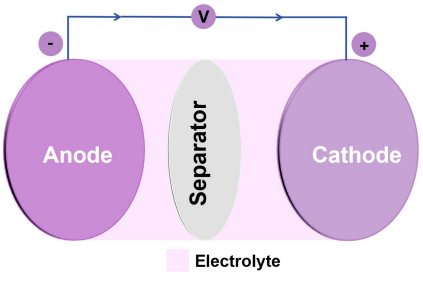


Figure 1 Schematic diagram of battery structure.

Received: November 28, 2025; **Revised:** December 19, 2025
Accepted: January 10, 2026

✉Address correspondence to liujunli@buaa.edu.cn

https://doi.org/10.26599/POM.2025.9140114

ones, have drawn particular attention. The sub-1 nm scale is close to the size of the unit cells of many crystalline compounds and the diameter of linear polymers/deoxyribonucleic acid chains [59–61]. Owing to their dimensions, near-100% surface atomic exposure, and large surface area, SNMs often exhibit unexpected physical and chemical properties (polymer-like behavior, flexibility, rheological behavior, etc.) [62–65] and excellent optical, electrical, and catalytic properties [66–71]. For example, SNMs provide structural advantages for energy storage in batteries. The abundant active sites of SNMs result in effective interactions with external fields and outstanding catalytic and energy storage properties. In addition, the sub-1 nm structures can shorten electron and ion diffusion pathways, increase the electrochemically active surface area, accelerate electrolyte penetration, alleviate the stress caused by volume expansion, and improve reaction dynamics [72]. Furthermore, POMs with well-defined structures usually exhibit good redox properties and can simultaneously donate and accept electrons, thus acting as electron sponges in catalytic reactions [73–83]. Hence, POM-based SNMs combining the advantages of POMs and SNMs hold promise as high-performance energy storage/conversion materials.

Given the scarcity of reviews on the use of POM-based SNMs in energy storage and conversion, we herein summarize progress in the controllable synthesis of POM-based SNMs and their applications in batteries (e.g., LIBs, SIBs, LOBs, ZABs, and Li–S batteries (LSBs)) and energy conversion (e.g., photothermal conversion, solar steam generation, and seawater desalination). Moreover, we outline the related development prospects and challenges and provide new insights for the design and application of SNMs.

2 Synthesis of POM-based SNMs

The precise design and controllable preparation of POM-based SNMs are of key importance for their energy storage/conversion applications. To date, SNMs have been fabricated using good and poor solvent strategies under hydrothermal/solvothermal conditions [84–87], physical exfoliation [88–90], chemical vapor deposition [91], etc. However, the synthesis of POM-based SNMs and component adjustment at the sub-1 nm scale remain challenging. Herein, we discuss the advanced synthetic routes to POM-based SNMs and selected successful cases.

2.1 Cluster–nuclei coassembly (CNCA)

Wang et al. (2019) proposed the CNCA strategy (Fig. 2(a)) [92], according to which POMs with well-defined structures and sizes at the sub-1 nm scale are introduced into a system containing inorganic materials and intervene in the nucleation process, limiting the size of inorganic nuclei to the sub-1 nm scale. As the size of sub-1 nm nuclei is comparable with that of POMs, they easily engage in CNCA driven by noncovalent (Coulomb and van der Waals) forces to afford POM-based SNMs. Thus, the CNCA method relies on the precise control of inorganic components at the sub-1 nm scale. Compared with the traditional LaMer model [92–94], the introduction of POMs limits the size of nuclei, which is a prerequisite for the subsequent formation of SNMs. In the LaMer pathway (Fig. 2(b)), the size of crystal nuclei is affected by surrounding molecules and nuclei and is difficult to limit to the sub-1 nm scale because of the propensity for explosive nucleation in the nucleation stage. Therefore, the CNCA strategy provides a notable advantage for SNM fabrication.

The CNCA strategy has been generalized to diverse POM-based low-dimensional SNMs, enabling the controllable design and fabrication of three-dimensional (3D) superlattice assemblies and two-dimensional (2D) and one-dimensional (1D) SNMs. 3D POM-based superlattice assemblies are typically prepared by introducing Mo-based POM clusters into Ni oxysulfide and Ni–Co hydroxide systems [92]. The introduction of Mo-based POMs into a NiS_x–NiO_x system was used to intervene in the nucleation process (Fig. 3(a)) and thus produce binary and ternary superlattice assemblies with highly ordered structures, as revealed by transmission electron microscopy (TEM) imaging (Figs. 3(b)–3(d)). These materials exhibited an extremely regular morphology and uniform elemental distribution. More surprisingly, the product particle shape and size were affected by the size of the introduced POM but not its type, which indicates that the size effect was the most important factor. The formation mechanism of these 3D superlattice assemblies was explored using molecular dynamics (MD) simulations. For Ni oxysulfide superlattice assemblies, these simulations (Figs. 3(e)–3(g)) suggest that a certain number of Ni oxysulfide molecules coassemble with POM clusters under the action of noncovalent forces. The coassembly of POMs and Ni oxysulfides provides building blocks that can further assemble and grow into larger 2D sub-1 nm nanosheets (SNSs). Under the action of polar solvents (e.g., ethanol), these SNSs assemble in a layer-by-layer fashion to form highly ordered 3D superlattice assemblies. The type of POM was found to influence the configuration of the layered structure (face-centered cubic, near-hexangular, and simple square patterns) but not the shape and size of product particles. This conclusion agrees with experimental results, proving the importance of the size effect of POMs.

The CNCA strategy can be expanded to fabricate 2D POM-

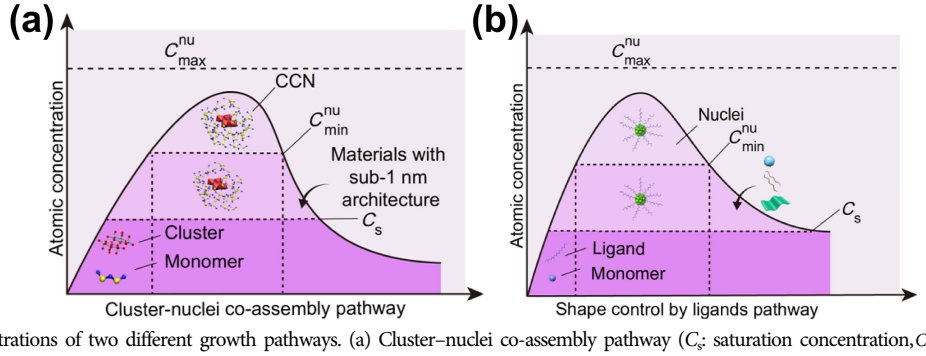


Figure 2 Schematic illustrations of two different growth pathways. (a) Cluster–nuclei co-assembly pathway (C_s: saturation concentration, C^{nu}_{min}: minimum nucleation concentration; C^{nu}_{max}: maximum nucleation concentration). (b) The LaMer pathway (wavy lines: 1D nanowires, green flake: 2D nanosheet, blue sphere: 3D nanospheres). Adapted with permission from Ref. [92], © Liu, J. L., under exclusive licence to Springer Nature Limited 2019.

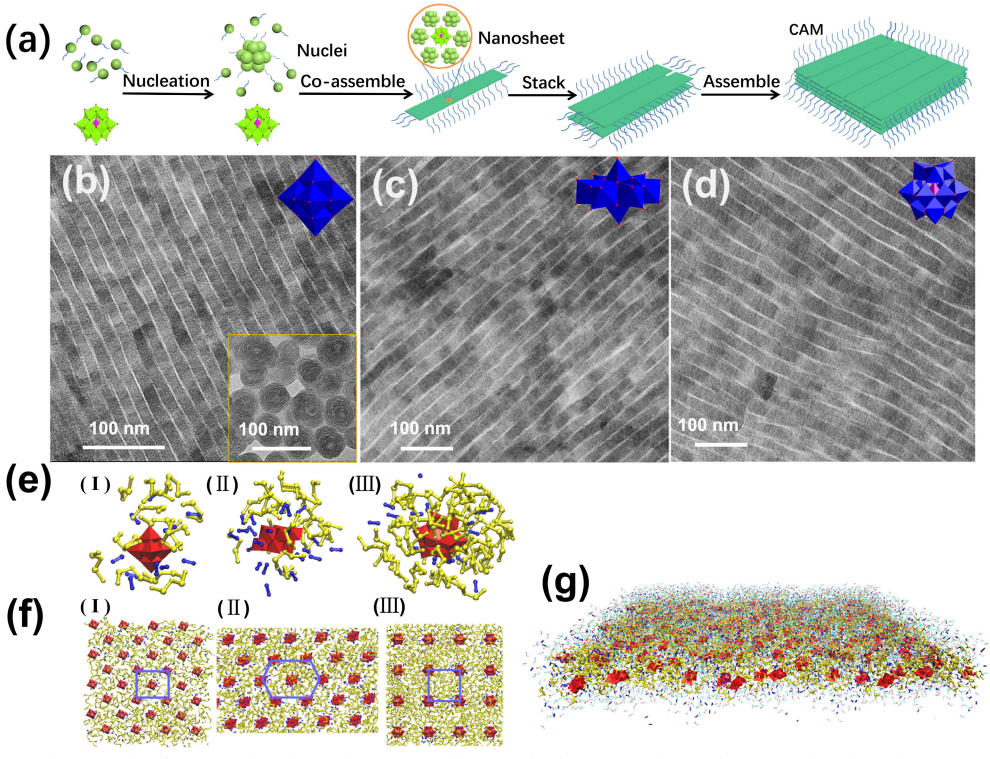


Figure 3 TEM images and MD results of 3D POM-based superlattice assemblies. (a) The formation scheme of 3D POM-based superlattice assemblies. TEM images of (b) NiS_x-NiO_x-Mo_6O_{19} assemblies (the inset is the TEM image of fullerene-like hollow nanospheres when POMs are absent from the nickel oxysulfide system), (c) NiS_x-NiO_x-Mo_8O_{26} assemblies, and (d) NiS_x-NiO_x-PMA assemblies. (e) Snapshot images (POM is in the core, Ni_3S_2 and NiO surround it to form the core-shell structure) of the MD results for building blocks of (I) Ni_3S_2-NiO-Mo_6O_{19}, (II) Ni_3S_2-NiO-Mo_8O_{26}, and (III) Ni_3S_2-NiO-PMA. (f) Snapshot images of the possible assembly morphologies of three kinds of materials: (I) Ni_3S_2-NiO-Mo_6O_{19}, (II) Ni_3S_2-NiO-Mo_8O_{26}, and (III) Ni_3S_2-NiO-PMA. Purple units highlight the denser facet centre cubic pattern, the near-hexangular pattern and the simple square pattern, respectively. (g) Simulated diagram obtained under periodical boundary conditions when 16 Ni_3S_2-NiO-Mo_8O_{26} with a near-hexagonal-pattern single layer were put into ethanol. Yellow, Ni_3S_2; dark blue, NiO; red, POMs; sapphire-pink, ethanol. Adapted with permission from Ref. [92], © Liu, J. L., under exclusive licence to Springer Nature Limited 2019.

based SNMs. Several sorts of 2D POM-based metal oxide SNSs were prepared, including CuO-POM (Figs. 4(a)–4(c)) [95], MnO-POM (Fig. 4(f)) [96], ZnO-POM (Figs. 4(g)–4(i)) [97], and $MnZnCuO_x$-POM (MZC-POM) (Figs. 4(j)–4(m)) [98] ones. To prepare the CuO-POM SNSs, phosphomolybdic acid (PMA) was incorporated into the CuO system during the nucleation stage. Under the action of noncovalent interactions, PMA coassembled with CuO to afford 2D SNSs. Atomic force microscopy (AFM) analysis (Fig. 4(d)) demonstrated that the CuO-PMA SNSs were ~ 1 nm thick, proving their sub-1 nm structure. The Fourier transform infrared spectra of the SNSs (Fig. 4(e)) featured the characteristic peaks of PMA, indicating that PMA maintained its structural integrity during the formation of the SNSs and stably existed therein. For MnO-POM and ZnO-POM SNSs, Mo and W-based POMs were introduced into MnO and ZnO systems. The type of POM did not affect product morphology, which agrees with the above conclusion regarding the importance of the size effect of POMs and confirms the universality of the CNCA method. Furthermore, based on the syntheses of CuO-, MnO-, and ZnO-POM SNSs, MZC-PMA SNSs were prepared. The SNS structure and catalytic performance could be precisely controlled by adjusting the amount of POM clusters, which lays a solid foundation for the fabrication of function-directed SNMs.

The fabrication of 3D and 2D POM-based SNMs has inspired the CNCA-based syntheses of 1D SNMs, such as nanobelts [99, 100] and nanowires [60, 64, 101]. Four kinds of 1D MoO_3-POM SNBs were prepared (Figs. 5(a)–5(d)). Four sorts of W-based POMs (W_6O_{19}, $W_{10}O_{32}$, $PW_{12}O_{40}$, and $SiW_{12}O_{40}$) were introduced into the MoO_3 system to obtain four hybrid sub-1 nm nanobelt superstructures (HSNSs) with similar morphologies. The MoO_3-POM HSNSs were highly ordered and flexible (Figs. 5(e)–5(h)), as follows from their capability to curl into loops. The CNCA method has been used to prepare various 1D sub-1 nm nanowires (SNWs), e.g., Au-POM, Fe_3O_4-POM, Y_2O_3-POM, Yb_2O_3-POM, Bi_2O_3-POM, and CeO_2-POM ones (Figs. 5(i)–5(p)). In the case of Au-phosphotungstic acid (Au-PW_{12}) SNWs, upon the introduction of PW_{12} into the Au system [60], Au coassembled with PW_{12} to form Au-PW_{12} SNWs with a diameter of ~ 1 nm and length of up to several micrometers (Figs. 5(i) and 5(k)–5(m)). These SNWs are the first example of an A-B-A-B copolymer-analogous structure. The corresponding cryo-electron microscopy image (Fig. 5(n)) featured bright–dark structures and revealed a size consistent with those of PW_{12} and Au clusters, directly confirming the A-B-A-B arrangement. Density functional theory (DFT) calculations confirmed the possibility and rationality of the A-B-A-B structure (Fig. 5(j)). This work opens up a new direction for constructing polymer-like structures from inorganic nanomaterials.

In addition to regulating material dimensions at the sub-1 nm scale, the CNCA strategy allows precise composition modulation (from single to multiple components). Wang and Liu designed and prepared 1D POM-based low-, medium-, and high-entropy SNWs (CeO_x-PMA (C-PMA), $ZrCeO_x$-PMA (ZC-PMA), $FeZrCeO_x$-PMA (FZC-PMA), $NiFeZrCeO_x$-PMA (NFZC-PMA), $CuNiFeZrCeO_x$-PMA (CNFZC-PMA), $ZnCuNiFeZrCeO_x$-PMA (ZCNFZC-PMA),

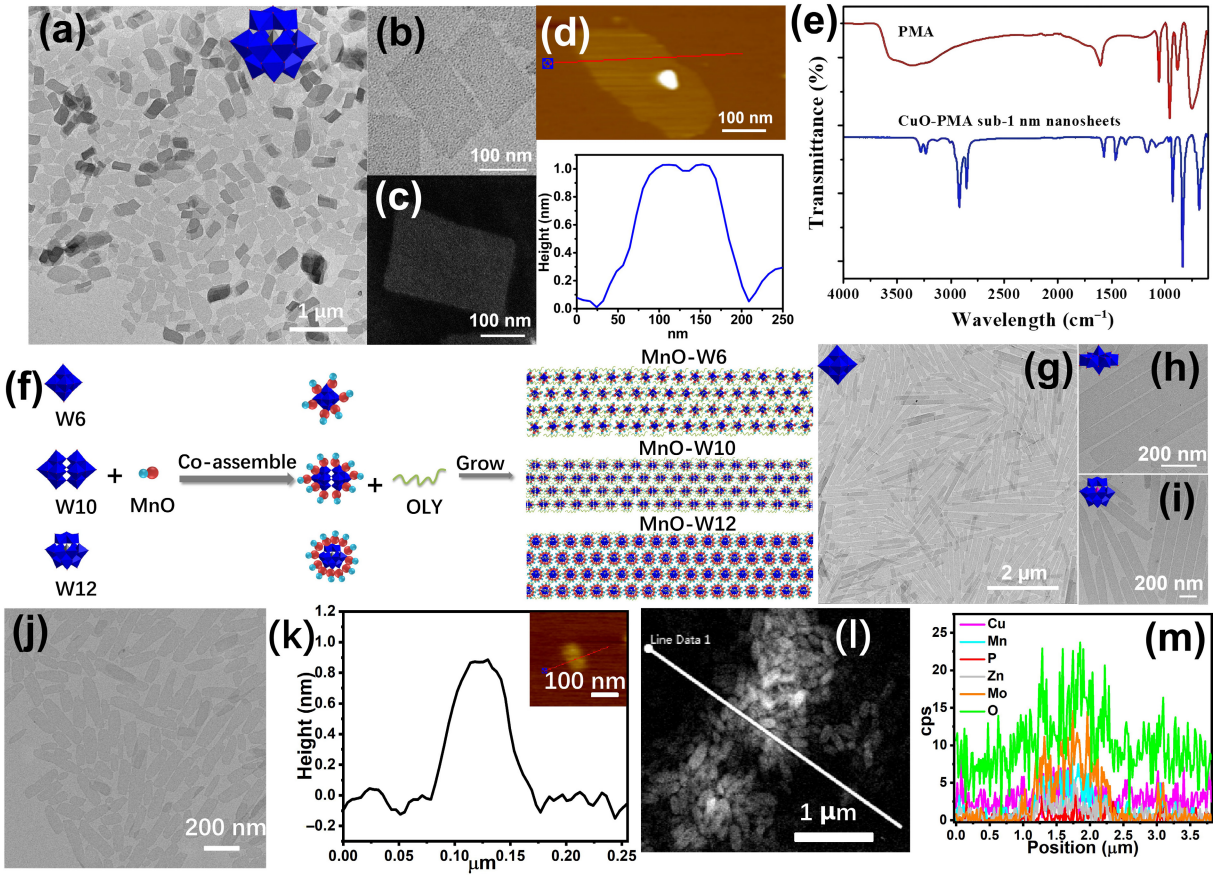


Figure 4 Characterizations of 2D POM-based SNMs. (a) and (b) TEM images of CuO-PMA SNSs (the inset is the PMA anion model). (c) The high angle annular dark field scanning transmission electron microscopy (HAADF-STEM) image of CuO-PMA SNSs. (d) The AFM pattern of CuO-PMA SNSs. (e) Fourier transform infrared spectroscopy (FT-IR) spectra of PMA and CuO-PMA SNSs. Adapted with permission from Ref. [95], © American Chemical Society 2019. (f) Schematic illustration of the assembly process of MnO-POM SNSs. (g)–(i) TEM images of the ZnO-Mo_6O_{19}, ZnO-Mo_8O_{26}, and ZnO-PMA 2D SNSs, respectively (the inset is the corresponding POM anion model). Adapted with permission from Ref. [97], © American Chemical Society 2021. (j) The TEM image of the MZC-PMA SNSs. (k) The AFM result of MZC-PMA SNSs. (l) The HAADF-STEM image and (m) corresponding energy dispersive X-ray spectroscopy (EDS) elemental line scan of MZC-PMA SNSs (the scanning direction was along the white line in (l)). Adapted with permission from Ref. [98], © Wiley-VCH GmbH 2023.

and CoZnCuNiFeZrCeO_x-PMA (CZCNFZC-PMA)) by introducing PMA clusters into metal oxide systems (Fig. 6) [102, 103]. With the increasing number of constituent elements, the SNW morphology remained unchanged (Figs. 6(a)–6(f)). Furthermore, owing to the sub-1 nm size effect, the obtained SNWs exhibited polymer-like properties (the inset in Fig. 6(d)). When the SNWs were dispersed in cyclohexane, bubbles were observed in the sample for a long time. Energy-dispersive X-ray spectroscopy (EDS) analysis (Figs. 6(g)–6(i)) showed that multiple elements were uniformly distributed throughout the SNWs, demonstrating the formation of 1D high-entropy oxide (HEO) SNMs.

HEO materials usually form at higher temperatures (> 900 K) and pressures (> 5 GPa) [104–106]. In the above work, HEO-PMA SNWs were obtained at 140 °C, which suggests that the introduction of POM clusters may play an important role in the production of HEO SNWs. Control experiments were conducted to explore the function of POM clusters during the formation of HEO SNWs. When various POM clusters were used instead of the PMA cluster, the SNWs still formed. However, SNW formation did not proceed in the absence of POM clusters. These results demonstrate the importance of POM clusters in the production of HEO SNWs. PMA clusters with an electron-rich structure act as effective carriers and linkers for various metal oxides, promoting their ordered arrangement and directional assembly and thereby facilitating the formation of HEO SNWs.

Beyond 1D HEO SNWs, the CNCA method can also be used to prepare 2D multicomponent and HEO SNSs [107]. PMA cluster incorporation afforded a material with a uniform sheet-like morphology (Figs. 7(a)–7(c)). AFM analysis (Fig. 7(d)) indicated that the SNSs were ~ 1 nm thick. Fourier transform extended X-ray absorption fine structure (FT-EXAFS) analysis (Fig. 7(e)) showed that Co, Fe, Ni, and Mn in the HEO SNSs had a similar coordination environment. EDS analysis (Fig. 7(f)) revealed the existence and uniform distribution of multiple elements in SNSs. Thus, all abovementioned techniques confirmed the preparation of 2D HEO SNSs.

2.2 Two-phase approach

The two-phase (aqueous and organic phases) approach is another typical strategy for synthesizing POM-based SNMs and can be applied at room temperature [63, 108]. Typically, POMs are dissolved in the aqueous phase, whereas quaternary ammonium salts are dissolved in the organic (chloroform) phase. The two phases are mixed upon stirring and centrifugation, and the organic phase is collected and allowed to naturally evaporate at room temperature to obtain a powder sample. Wang et al. dissolved $K_{10}P_2W_{17}O_{61}$ and $AgNO_3$ in aqueous phases, dissolved cetyltrimethylammonium bromide (CTAB) in chloroform

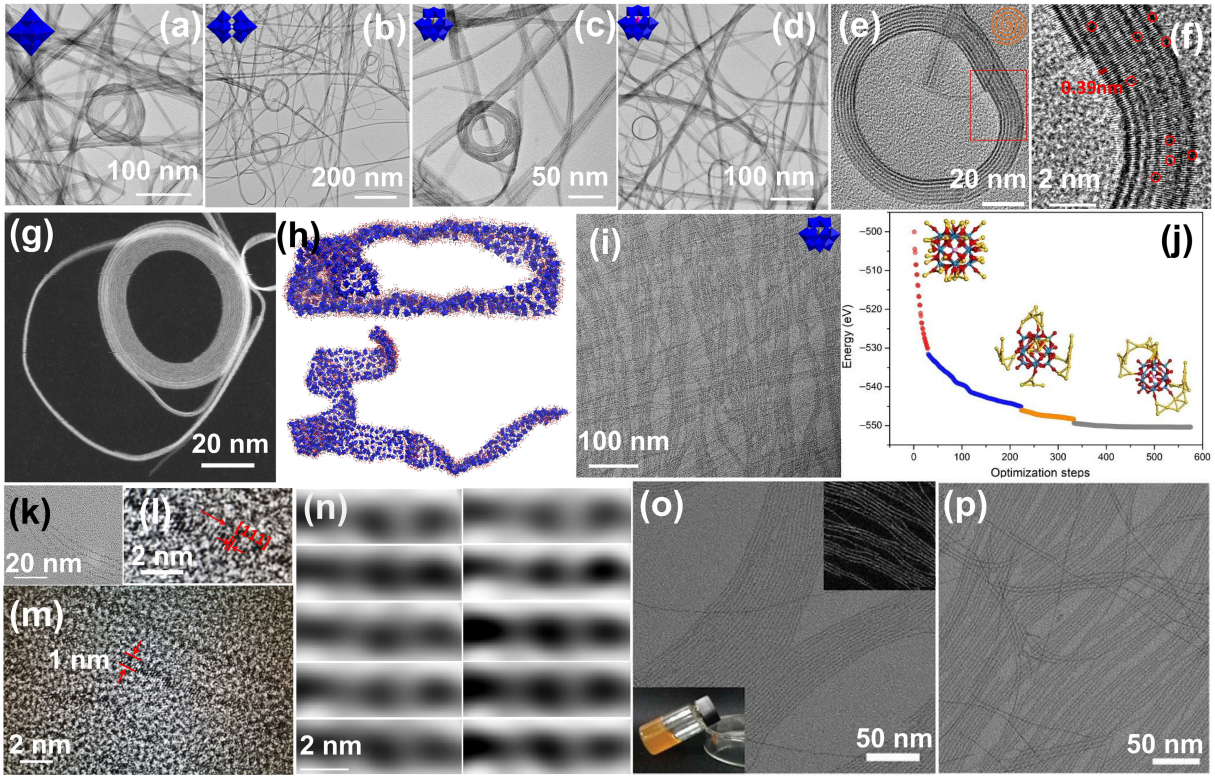


Figure 5 Characterizations of 1D POM-based SNMs. TEM images of (a) MoO_3-W_6O_{19} HSNSs, (b) MoO_3-$W_{10}O_{32}$ HSNSs, (c) MoO_3-$PW_{12}O_{40}$ HSNSs, and (d) MoO_3-$SiW_{12}O_{40}$ HSNSs (the inset: The blue model corresponds to the W_6O_{19}, $W_{10}O_{32}$, $PW_{12}O_{40}$, and $SiW_{12}O_{40}$ anion model, respectively). (e) Cryo-EM image of MoO_3-W_6O_{19} HSNSs (the inset is the model of HSNSs). (f) Magnified Cryo-EM image of the red frame part in (e). (g) HAADF-STEM image of the MoO_3-W_6O_{19} HSNSs. (h) After the MD simulations, the MoO_3-W_6O_{19} HSNSs formed a circle and the side view of 114 nm length MoO_3-W_6O_{19} HSNSs formed a helical ribbon. Adapted with permission from Ref. [99], © American Chemical Society 2020. (i) TEM image of Au-PW_{12} SNWs dispersed in chloroform (the inset of top right corner is the PW_{12} anion model). (j) The energy–structure correlation trend based on the 575 optimization steps during DFT optimizations starting from the initial model structure with the 36 Au atoms averagely connecting to the 36 oxygen sites on the surface of the $[PW_{12}O_{40}]^{3-}$. Colors: Au (yellow), O (red), W (blue), P (pink). (k)–(m) The high-resolution transmission electron microscopy (HRTEM) images of Au-PW_{12} SNWs dispersed in chloroform. (n) The 2D average of the Au-PW_{12} SNWs obtained by Cryo-EM (the Au-PW_{12} SNWs were dispersed into ethanol). Adapted with permission from Ref. [60]. © Wiley-VCH GmbH 2020. TEM images of SNWs: (o) Fe_3O_4-PMoO and (p) Y_2O_3-PMoO SNWs. Adapted with permission from Ref. [101], © Wiley-VCH GmbH 2021.

respectively, to obtain 1D Ag-P_2W_{17} SNWs (Figs. 8(a)–8(c)) [108]. During synthesis, visible light can promote the reduction of Ag^+ on the POM surface to form Ag clusters. In the two-phase system, POMs can bind to metal ions through electrostatic interactions. This binding leads to an uneven charge distribution on the surface of POMs, facilitating their directional assembly with metal clusters. CTAB encapsulates POM–metal assemblies via electrostatic interactions, neutralizes a part of the charge, and ensures the distribution of the assemblies in the aqueous phase. The long alkyl chains of CTAB are exposed and present in chloroform. The two-phase equilibrium is maintained by Coulombic and intermolecular forces (Fig. 8(d)).

The two-phase method was used to prepare 2D SNMs. An aqueous solution of $[NdPW_{11}O_{39}]^{3-}$ was mixed with a chloroform solution of a quaternary ammonium salt, and a monolayer clusterphene structure was obtained at a certain ionic strength and reaction time (Fig. 8(e)) [109]. High-resolution aberration-corrected TEM imaging (Fig. 8(f)) revealed the presence of closely connected monolayer clusterphene units. This structure exerted an electron delocalization effect, thereby resulting in excellent catalytic performance. Moreover, different morphologies could be obtained by regulating the ionic strength or reaction time. At a short reaction time or low ionic strength, multilayer clusterphene products were obtained (Fig. 8(g)). At a high ionic strength or long reaction time, nanobelt structures were obtained (Fig. 8(h)). AFM analysis (Fig. 8(i)) indicated that the average nanobelt thickness was ~ 3 nm. Upon an increase in ionic strength, the nanobelts became shorter, while their width and thickness remained unchanged. Product morphology was affected by the type of the quaternary ammonium salt. Quaternary ammonium salt ions with short alkyl chains did not support 2D structure formation and hence, the establishment of clusterphene structures.

1D sub-1 nm structures synthesized by the two-phase method can form 3D structures through stacking. In a representative study, Eu-substituted Wells-Dawson–type POM clusters (1.2 nm in length and 1 nm in height) (Fig. 8(j)) were used as precursors, with Eu in the POMs substituted by 15 types of transition metals and lanthanides [110]. K acetate acted as a molecular linker, promoting the assembly of POM molecules. When the solution pH exceeded 6.5, the material assembled into 1D SNWs at the two-phase interface (Fig. 8(k)). At pH < 4, sub-1 nm nanorings (SNRs) were formed (Fig. 8(l)), subsequently self-assembling into nanocolumns (Fig. 8(m)) and finally forming a 3D superstructure (Fig. 8(n)).

3 Applications of POM-based SNMs in energy storage

Long-term reliance on nonrenewable resources may lead to their

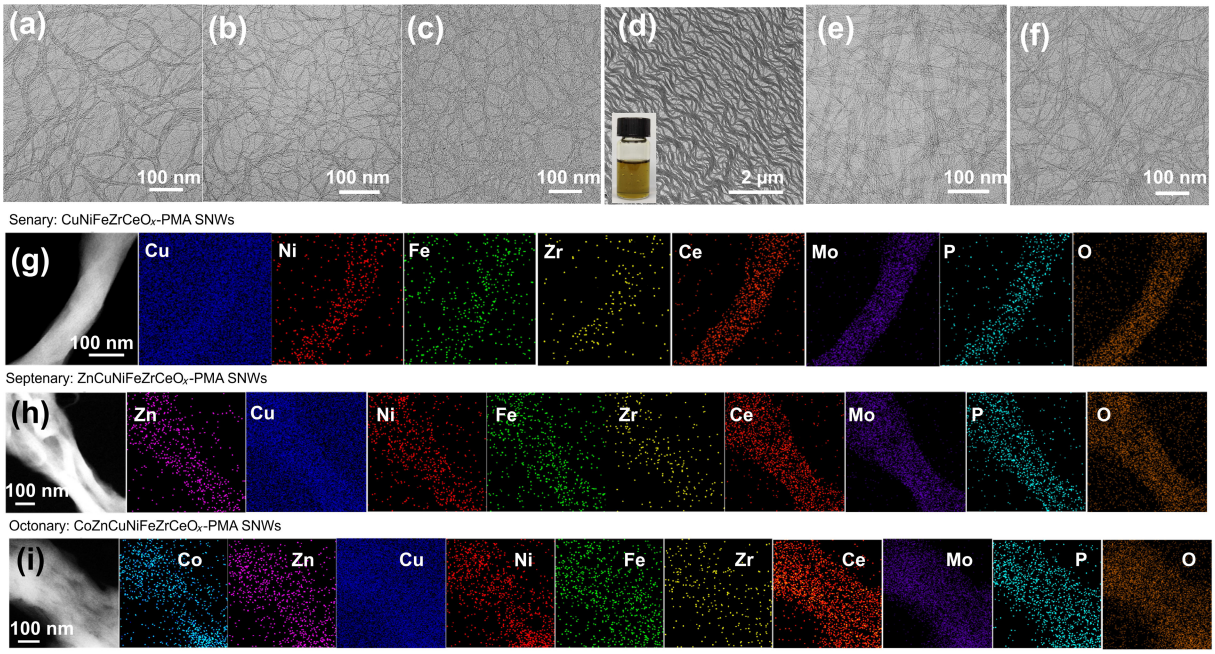


Figure 6 Morphological images of 1D HEO-POM SNWs. TEM images of (a) C-PMA SNWs, (b) ZC-PMA SNWs, (c) NFZC-PMA SNWs, (d) CNFZC-PMA SNWs (the inset is the cyclohexane dispersion with polymer-like property), (e) ZCNFZC-PMA SNWs, and (f) CZCNFZC-PMA SNWs. (g) The HAADF-STEM image and corresponding EDS elemental mappings of CNFZC-PMA SNWs. (h) The HAADF-STEM image and corresponding EDS elemental mappings of ZCNFZC-PMA SNWs. (i) The HAADF-STEM image and corresponding EDS elemental mappings of CZCNFZC-PMA SNWs. Adapted with permission from Ref. [62] © American Chemical Society 2022.

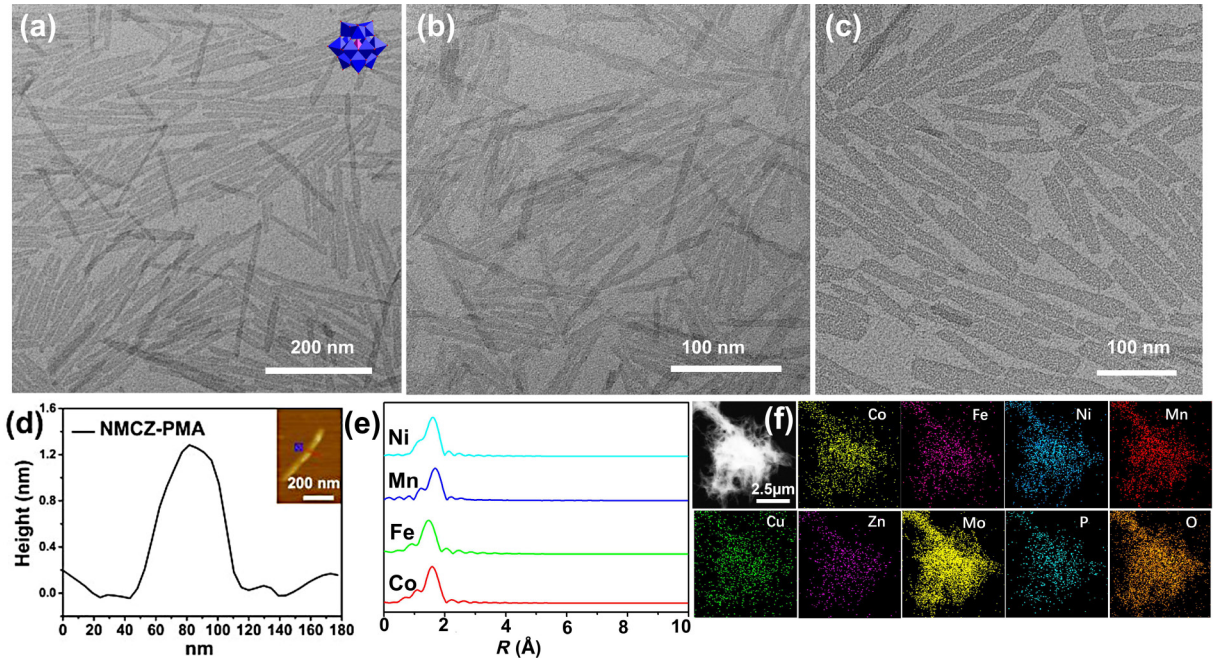


Figure 7 Characterizations of 2D HEO-POM SNSs. TEM images of the (a) NiMnCuZnO$_x$-PMA (NMCZ-PMA) SNSs, (b) FeNiMnCuZnO$_x$-PMA (FNMCZ-PMA) SNSs, and (c) CoFeNiMnCuZnO$_x$-PMA (CFNMCZ-PMA) SNSs. (d) AFM result of the NMCZ-PMA SNSs. (e) FT-EXAFS spectra of Ni, Mn, Fe, and Co in CFNMCZ-PMA SNSs. (f) The HAADF-STEM image and corresponding elemental mappings of the CFNMCZ-PMA SNSs. Adapted with permission from Ref. [107], © American Chemical Society 2024.

depletion. Renewable resources such as wind energy, solar energy, and hydropower are abundant, cheap, and environmentally friendly but intermittent and should therefore be converted into a storable form for efficient utilization. Batteries are widely used as energy storage devices. The voltaic pile, developed in 1800, was the world's first battery, proving that chemical energy can be converted into electrical energy [111]. The development of the Daniell cell (1836) solved the problem of electrode polarization and made notable progress in overcoming the problem of overpotential [112]. The Leclanché cell (1886) achieved a breakthrough in electrolyte composition. Unlike previous cells, which used liquid electrolytes, it used a paste electrolyte and zinc as the negative electrode and

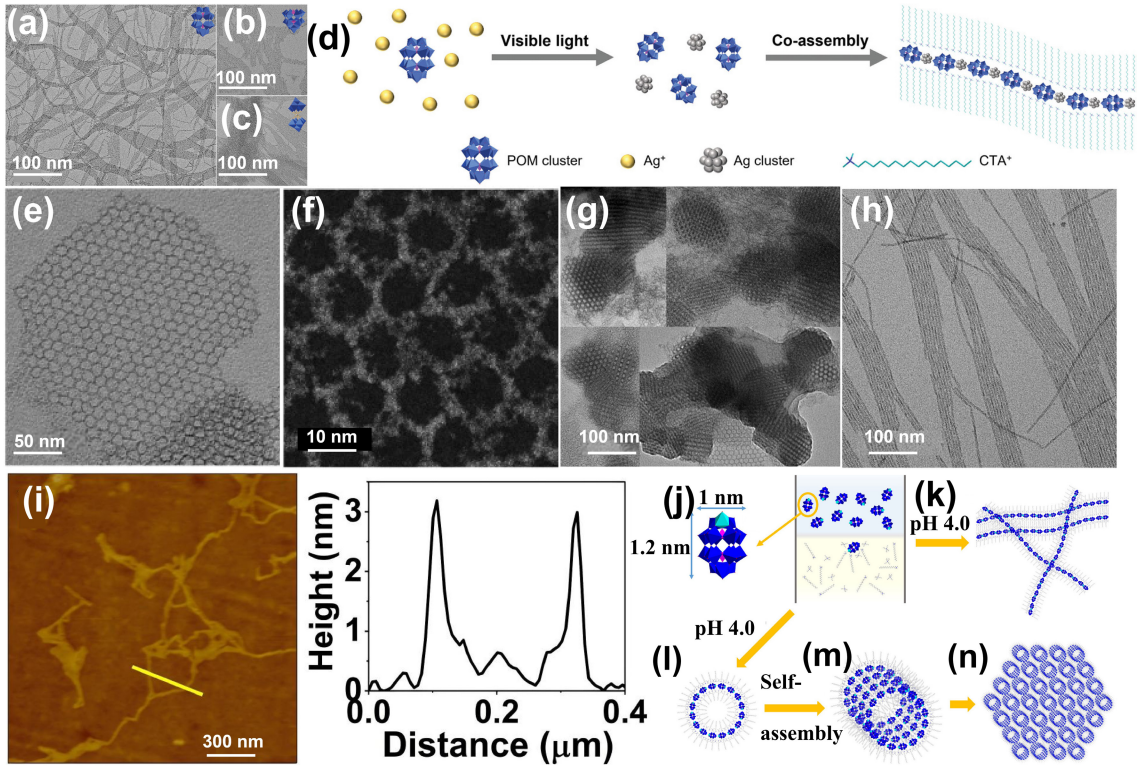


Figure 8 POM-based SNMs synthesized by two-phase approach. (a) TEM image of Ag-P_2W_{17} SNWs (the inset is the structure of $[P_2W_{17}O_{62}]^{10-}$ cluster). (b) TEM image of Ag-P_2W_{15} SNWs (the inset is the structure of $[P_2W_{15}O_{56}]^{12-}$ cluster). (c) TEM image of Ag-EuW_{10} SNWs (the inset is the structure of $[EuW_{10}O_{36}]^{9-}$ cluster). (d) Illustration of the synthetic procedure toward Ag-POM SNWs. Red: O; blue: W; pink: P; yellow: Ag^+; gray: Ag cluster; cyan: CTA^+. Adapted with permission from Ref. [108], © Wiley-VCH GmbH 2022. (e) TEM image of monolayer clusterphenes. (f) High-resolution aberration-corrected TEM image of monolayer clusterphenes. (g) TEM images of multilayer clusterphenes. (h) TEM image of ultrathin nanobelts with different aspect ratios. (i) AFM result of $NdPW_{11}$ ultrathin nanobelts. Adapted with permission from Ref. [109], © Liu, Q. D. et al., some rights reserved; exclusive licensee American Association for the Advancement of Science. No claim to original U.S. Government Works 2019. (j) Dawson-type POM cluster. (k) Single-cluster nanowires. (l) Single-cluster nanoring. (m) Nanocolumn constructed by nanorings. (n) 3D superstructure assembled by nanorings. Adapted with permission from Ref. [110], © Liu, Q. D. et al., some rights reserved; exclusive licensee American Association for the Advancement of Science. No claim to original U.S.Government Works. Distributed under a Creative Commons Attribution NonCommercial License 4.0 (CC BY-NC) 2019.

container, thus representing the first portable battery [113]. All the above batteries are primary (i.e., nonrechargeable and nonreusable) batteries. The first rechargeable battery is the lead–acid battery, which was reported in 1859 [114]. When the voltage drops to a certain value, this battery can be recharged in reverse. However, lead–acid batteries are large and inconvenient to carry, and better alternatives are therefore required.

Technical progress places increasingly stricter requirements on batteries. Devices such as watches, mobile phones, and laptops require batteries to be portable and rapidly chargeable, whereas electric vehicles prioritize high capacity. A battery usually consists of a positive electrode, negative electrode, electrolyte, and separator. The performance of batteries can be enhanced by developing novel battery component materials, with smaller-sized materials often leading to higher performance [115]. At the sub-1 nm scale, the surface atom exposure is close to 100%, which results in more abundant active sites, higher catalytic activity, and stronger effects of external fields. Owing to their sub-1 nm structure, electron-rich nature of POMs, and synergistic effect of multiple components [116], POM-based SNMs exhibit high activity and stability, thus being promising energy storage materials, as outlined below.

3.1 Metal-ion batteries

A metal-ion battery uses metal ions as charge carriers and realizes the storage and release of electrical energy through the transfer of these ions between the positive and negative electrodes. The most extensively studied metal-ion batteries are LIBs and SIBs.

3.1.1 *LIBs*

The small atomic mass of Li endows LIBs with high gravimetric and volumetric energy densities [117–121]. Moreover, the small radius of Li ions allows for their rapid diffusion-based migration in electrode materials, resulting in a high charge–discharge efficiency [122–125]. More importantly, LIBs have the potential for high energy output and ion transport performance, thus being suitable for high-power-demand scenarios [126–128]. LIBs are widely used to power smartphones, laptops, smart watches, and other portable modern electronic devices [129–131] but face numerous challenges. For instance, transition metal oxide-based anode materials experience considerable volume expansion during the repeated intercalation and deintercalation of Li ions [132–135], which not only affects the structural stability of the electrode but also decreases battery discharge capacity. Therefore, new high-performance battery materials should be developed through reasonable material design and structural optimization to suppress the adverse effects of volume expansion, enhance electrochemical stability, and thus improve LIB performance [98, 136–138].

As LIB anode materials, MZC-PMA SNSs (Figs. 9(a)–9(c)) have been fabricated by introducing PMA clusters into the MZC system [98], with POMs coassembling with MZC and growing into 2D

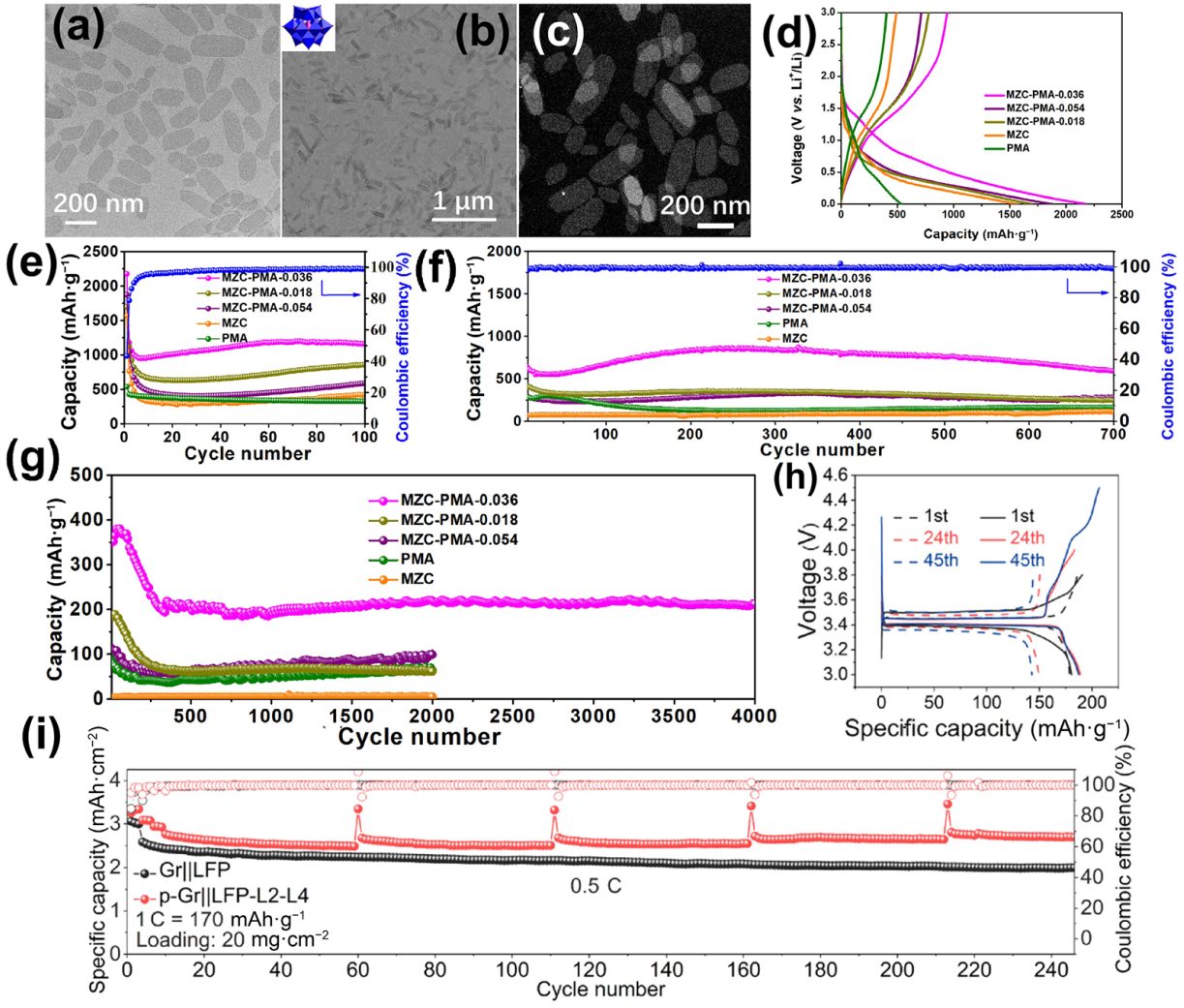


Figure 9 2D MZC-PMA SNSs as anode in LIBs. (a) and (b) TEM images of the MZC-PMA SNSs (the inset is the PMA model). (c) The HAADF-STEM image of MZC-PMA SNSs. (d) Galvanostatic initial discharge/charge curves for three kinds of MZC-PMA SNSs, MZC and PMA at 100 mA·g^{-1}. Long-term cycling tests of three kinds of MZC-PMA SNSs, MZC and PMA at (e) 100 mA·g^{-1}, (f) 1.0 A·g^{-1}, and (g) 3.0 A·g^{-1}. Adapted with permission from Ref. [98], © Wiley-VCH GmbH 2023. (h) Charge–discharge curves at the current density of 0.5 C. (i) Cycling performance under different voltage activation (LFP: $LiFePO_4$; LFP-L2-L4: Mo-W@BNC-L2-L4; p-Gr: pre-lithiated graphite). Adapted with permission from Ref. [121], © Wiley-VCH GmbH 2025.

SNSs under the action of Coulomb and van der Waals forces. When used in LIB anodes, this special 2D sub-1 nm structure generates abundant active sites and mitigates the impact of volume expansion during charge–discharge. The synergistic effect of multiple metal oxides and POMs further enhances LIB performance. DFT calculations show that the presence of electron-rich POMs improves the energy of Li-ion adsorption on MZC-PMA SNSs, thus accelerating the Li-ion migration rate and enhancing battery performance. Therefore, MZC-PMA SNSs are superior to Mo-W@BNC as a LIB anode material (Figs. 9(h) and 9(i)) [121]. At a current density of 100 mA·g^{-1}, MZC-PMA SNS-based LIBs deliver a very high initial discharge capacity of 2177 mAh·g^{-1} (Fig. 9(d)) and maintain a specific discharge capacity of 1157 mAh·g^{-1} during 100 cycles at 100 mA·g^{-1} (Fig. 9(e)). After 700 cycles at 1.0 A·g^{-1}, the specific discharge capacity reaches 592 mAh·g^{-1} (Fig. 9(f)). At 3.0 A·g^{-1}, the material sustains 4000 cycles and exhibits a specific discharge capacity of 212 mAh·g^{-1} (Fig. 9(g)).

Tan et al. hydrothermally prepared a novel (nongraphite) anode material [138], namely a PMo_{12}/CoTPyP composite, by exploiting the interaction of PMo_{12} with porphyrin (Fig. 10(a)). Porphyrins are π-conjugated aromatic molecules with delocalized molecular orbitals, structural diversity, and multiple active sites. The internal electron cloud of PMo_{12}/CoTPyP forms a sub-1 nm channel for Li^+ transport, which can reduce the energy barrier of Li^+ migration (Figs. 10(b)–10(d)) and thus accelerate the same. At a current density of 0.125 A·g^{-1}, the PMo_{12}/CoTPyP anode delivered a specific discharge capacity of 1398 mAh·g^{-1} (Fig. 10(e)). This performance exceeds that of most reported POM- and porphyrin-based anode materials. After 800 cycles, this anode maintained a discharge capacity of 936 mAh·g^{-1} (Fig. 10(f)).

Most LIBs use liquid electrolytes, which, however, are flammable and therefore pose safety risks [139–141]. In addition, liquid electrolytes often engage in chemical reactions with metallic Li in the battery anode, which causes interface instability and exacerbates safety risks [142–144]. These issues can be addressed through the use of solid electrolytes, which usually comprise inorganic or organic solid materials and feature high thermal stability and mechanical strength and therefore enhance battery safety [145–147]. Nevertheless, solid electrolytes generally exhibit low ionic conductivity and hence, low Li-ion migration rates [148–150].

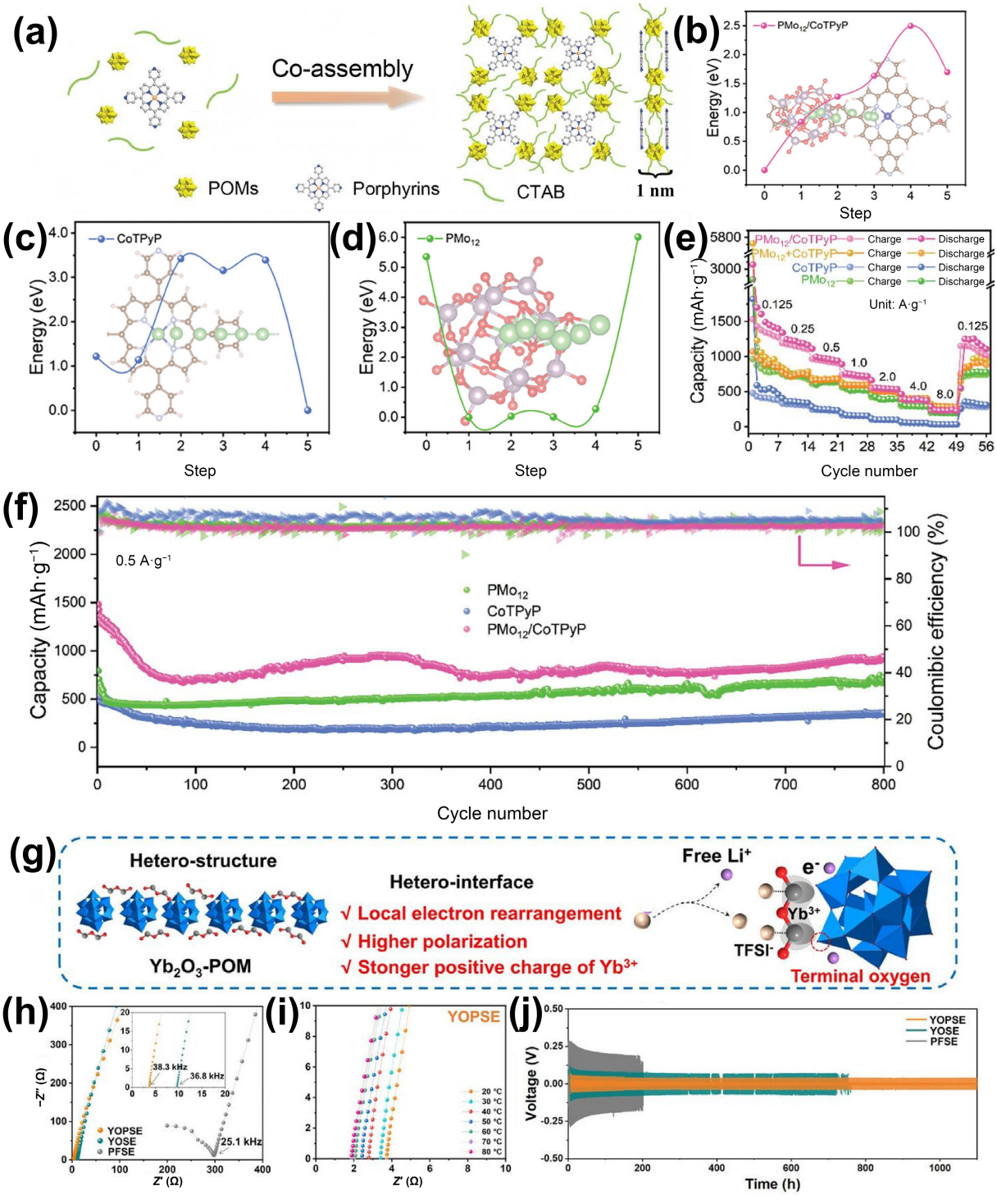


Figure 10 The battery performance of PMo_{12}/CoTPyP co-assembled hybrid nanomaterials and Yb_2O_3-POM heterogeneous cluster chains. (a) Schematic diagram of the synthetic process of POMs/porphyrin hybrid nanomaterials. The simulated migration energy barrier of Li^+ on (b) PMo_{12}/CoTPyP, (c) CoTPyP, and (d) PMo_{12}. (e) Rate performances of PMo_{12}/CoTPyP, PMo_{12}+CoTPyP, CoTPyP, and PMo_{12}. (f) Long-term cycling tests of PMo_{12}/CoTPyP, CoTPyP, and PMo_{12} at 0.5 A·g^{-1} for 800 cycles. Adapted with permission from Ref. [138], © Wiley-VCH GmbH 2024. (g) YOP and their interaction with lithium-salt. EIS plots of (h) solid state electrolytes (SSEs) at room temperature and (i) YOP SSEs at different temperatures (YOSE: Yb_2O_3 SSEs and PFSE: PVDF-HFP SSEs). (j) Galvanostatic Li plating/stripping profiles of Li symmetric cell at 0.1 mA·cm^{-2} for 1100 h. Adapted with permission from Ref. [137], © Wiley-VCH GmbH 2025.

Moreover, the poor interfacial compatibility of solid electrolytes and electrode materials results in increased interfacial impedance and hence, reduced cycle life and efficiency [151, 152].

The ionic conductivity and safety of solid electrolytes should be improved to promote the use of LIBs in electric vehicles, portable electronic devices, and large-scale energy storage systems and thus advance clean energy technologies. Xu et al. exploited van der Waals forces to synthesize Yb_2O_3-POM heterogeneous cluster chains (YOP) under hydrothermal conditions [137]. Owing to their electron-withdrawing properties, the terminal oxygen atoms of

PMA captured electrons from Yb_2O_3 and caused local electron rearrangement at YOP. Yb^{3+} combined with bis(trifluoromethanesulfonyl) imide ($TFSI^-$) and released more Li^+, thus promoting Li^+ transport (Fig. 10(g)). At room temperature and 60 °C, the ionic conductivity was 0.68 mS·cm^{-1} (Fig. 10(h)) and 1.2 × 10^{-3} mS·cm^{-1} (Fig. 10(i)), respectively. At a current density of 0.1 mA·cm^{-2}, the material in a symmetric LI cell sustained 1100 h of operation (Fig. 10(j)).

3.1.2 SIBs

Compared with Li resources, Na ones are extremely abundant, widely distributed, and therefore cheaper to acquire and extract, which makes SIBs ideal alternatives to LIBs [153–155]. However, the intercalation/deintercalation of Na ions into/from the electrode during SIB operation results in kinetic limitations [156–158], triggers irreversible phase transition reactions, and may even cause the structural damage or collapse of electrode materials, seriously affecting the battery cycle life and rate performance. The development of electrode materials supporting the rapid migration and stable storage of Na ions would notably enhance the overall electrochemical performance of SIBs. POM-based SNMs show great potential in this regard because of their unique structural characteristics. On the one hand, these materials possess abundant and highly dispersed active sites, thus having the capacity to shorten the transmission paths of Na ions and electrons and thereby enhance charge–discharge efficiency and rate performance. On the other hand, the electron-rich POM groups can undergo reversible redox reactions during electrochemical processes, providing an additional charge storage mechanism and thus further improving battery capacity and stability. These structural advantages make POM-based SNMs highly promising electrode materials for SIBs.

Wang et al. synthesized POM-based HEO SNWs via the CNCA method [103]. PMA interacted with metal oxides under the influence of Coulomb and van der Waals forces, which resulted in the growth of nanowires with a diameter of 1 nm (Figs. 6(a)–6(f) and 11(a)). The morphology of SNWs did not change with the increasing number of metals. As the number of metals increased from one to seven, the electrochemical performance of the POM-based SNWs as anode materials in SIBs improved (Fig. 11(b)), which highlights the impact of the entropy modulation effect on battery performance. At a current density of 0.1 C (30 mA·g^{-1}), the specific discharge capacity of CZCNFZC-PMA SNW-based SIBs reached 305 mAh·g^{-1} (Fig. 11(c)), notably exceeding that of C-PMA SNWs-based SIBs. At 10 C, CZCNFZC-PMA SNW-based SIBs could be stably operated for 5000 cycles, delivering a capacity retention of 92% (Fig. 11(d)). Compared with previously reported materials, CZCNFZC-PMA SNWs provided advantages in terms of rate performance and cycle stability at high current densities, which demonstrates the potential of HEO POM-based SNMs as SIB components.

3.2 Metal–air batteries

Metal–air batteries offer the advantages of high energy density, high safety, and excellent ecofriendliness [159–162] but face numerous technical challenges hindering practical applications. For instance, the sluggish kinetics of charge–discharge reactions lead to low cathode reaction efficiencies [163–165], while the adhesion of discharge products to the electrode surface results in short cycle

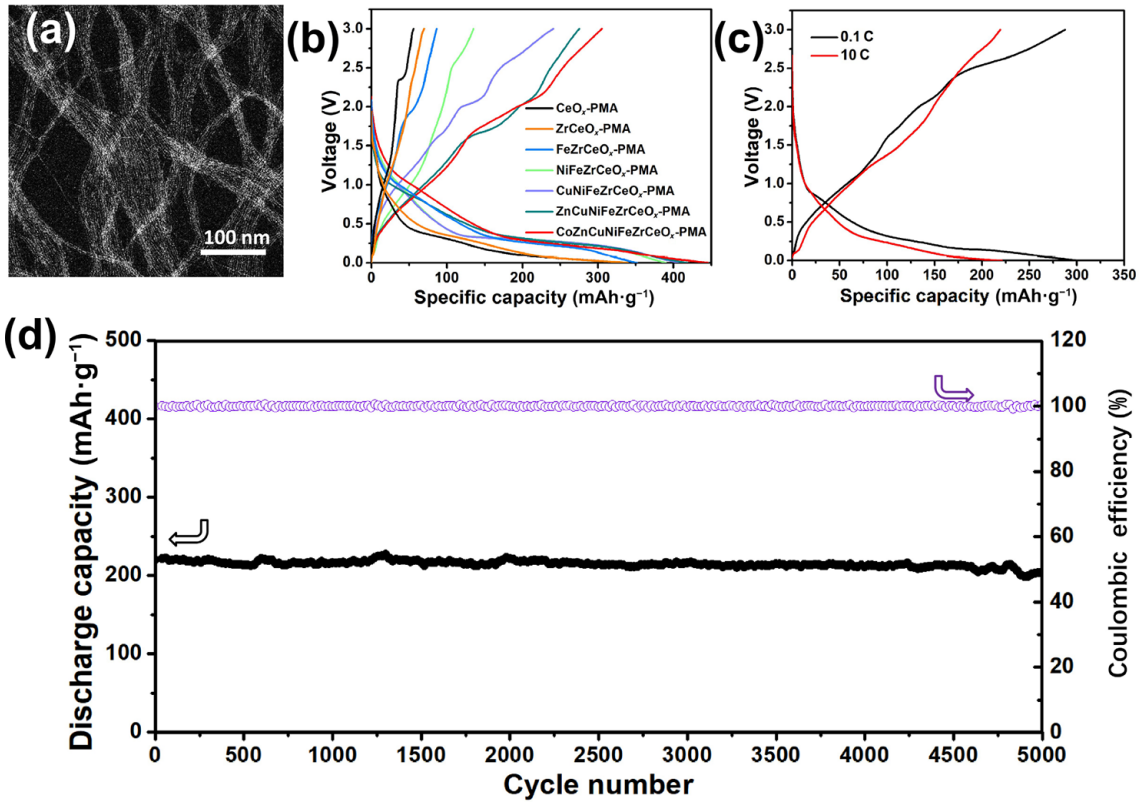


Figure 11 POM-based multiple metal oxide SNWs as anode in SIBs. (a) The HAADF-STEM image of CZCNFZC-PMA SNWs. (b) Galvanostatic initial discharge/charge curves for seven kinds of POM-based multiple metal oxide SNWs at a current density of 0.1 C. (c) Galvanostatic discharge/charge curves (the second cycle) of CZCNFZC-PMA SNWs-based SIBs at 0.1 C and 10 C, respectively. (d) Cycling stability of CZCNFZC-PMA SNWs-based SIBs at 10 C. Adapted with permission from Ref. [62], © American Chemical Society 2022.

清華大学出版社 Tsinghua University Press | SciOpen

lifetimes [166–170]. As cathode catalysts, POM-based SNMs can effectively enhance the performance of metal–air batteries [102, 107]. The high atomic exposure rate of POM-based SNMs results in abundant catalytic sites and hence, enhanced reaction kinetics, while the noncovalent interaction of POMs and inorganics and the synergetic effect of multiple components can further prolong battery lifetime.

3.2.1 LOBs

LOBs have attracted widespread attention because of their high theoretical energy density (3500 Wh·kg^{-1}) [25, 171, 172]. The performance of such batteries can be enhanced through the use of nanomaterials [173–177]. In LOBs, Li foil is used as the anode (Fig. 12(a)). During the battery reaction, Li ions in the electrolyte undergo redox reactions with O_2 to generate insulating Li_2O_2. The discharge products adhere to the cathode surface and hinder the battery reaction, decelerating the oxygen reduction reaction (ORR) and oxygen evolution reaction (OER), increasing the overpotential, and decreasing battery lifetime [178–180]. When used as cathode catalysts, POM-based SNMs can enhance battery performance by improving reaction kinetics [102]. On the one hand, the presence of electron-rich POMs in SNMs facilitates the adsorption of LiO_2 as the reaction intermediate. On the other hand, the sub-1 nm structure of POM-based SNMs increases the exposure rate of surface atoms and thus, the number of active sites for the OER and ORR. Consequently, as cathode catalysts for LOBs, POM-based SNMs outperform bulk materials.

Liu et al. synthesized POM-based metal oxide SNWs using the CNCA strategy (Fig. 13(a)) and applied them as cathode catalysts in LOBs, achieving outstanding battery performances [102]. The number of metal oxides ranged from one to six, and the corresponding SNWs included BiO_x-PMA (BO_x-PMA), $BiCuO_x$-PMA (BCO_x-PMA), $BiCuFeO_x$-PMA ($BCFO_x$-PMA), $BiCuFeCeO_x$-PMA ($BCFCO_x$-PMA), $BiCuFeCeWO_x$-PMA ($BCFCWO_x$-PMA), $BiCuFeCeWNiO_x$-PMA ($BCFCWNO_x$-PMA), $BiCuFeCeWMnO_x$-PMA ($BCFCWMO_x$-PMA), and $BiCuFeCeWPtO_x$-PMA ($BCFCWPO_x$-PMA) ones. With the increasing number of metals, the specific discharge capacity and cycle life of LOBs increased. The highest discharge capacity was observed for $BCFCWO_x$-PMA SNWs and attributed to the synergistic effect of multiple components and entropy modulation effect (Fig. 13(b)). The battery performance was further optimized by adjusting the components of HEO SNWs. Three sorts of HEO SNWs were prepared, including six kinds of metal oxides. $BCFCWPO_x$-PMA SNW-based LOBs exhibited the highest specific discharge capacity (11,206 mAh·g^{-1}), outperforming LOBs based on $BCFCWMO_x$-PMA SNWs (9267 mAh·g^{-1}) and $BCFCWNO_x$-PMA SNWs (8007 mAh·g^{-1}) (Fig. 13(c)). The $BCFCWPO_x$-PMA SNW-based LOBs could be stably cycled for 213 cycles and had a lifetime of ~ 1800 h (Figs. 13(b) and 13(e)). This performance was superior to that achieved using single-atom catalysts (CNT@Ru) (Fig. 13(h)) [181]. DFT calculations showed that the energy of LiO_2 adsorption on $BCFCWPO_x$-PMA SNWs exceeds that on $BCFCWPO_x$ (Figs. 13(f) and 13(g)). LiO_2, as a reaction intermediate, plays a crucial role in determining the deposition behavior of the discharge product (Li_2O_2). Therefore, the higher energy of LiO_2 adsorption on

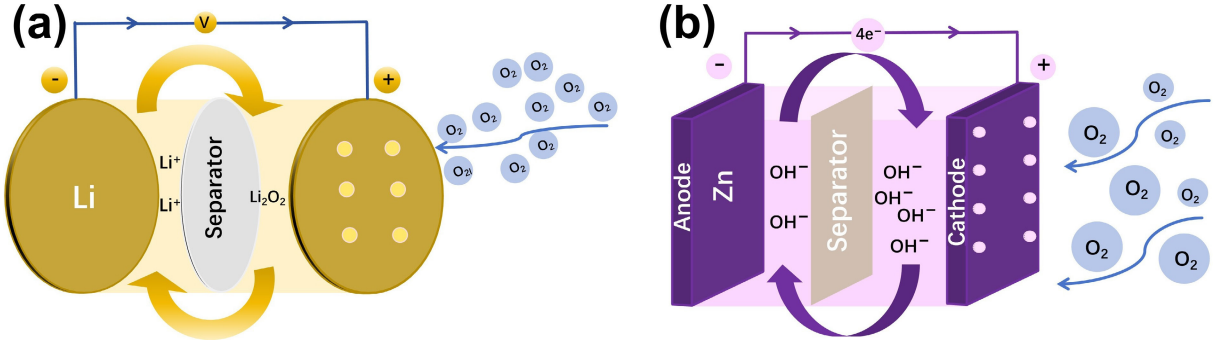


Figure 12 Metal–air battery models. (a) LOBs model. (b) ZABs model.

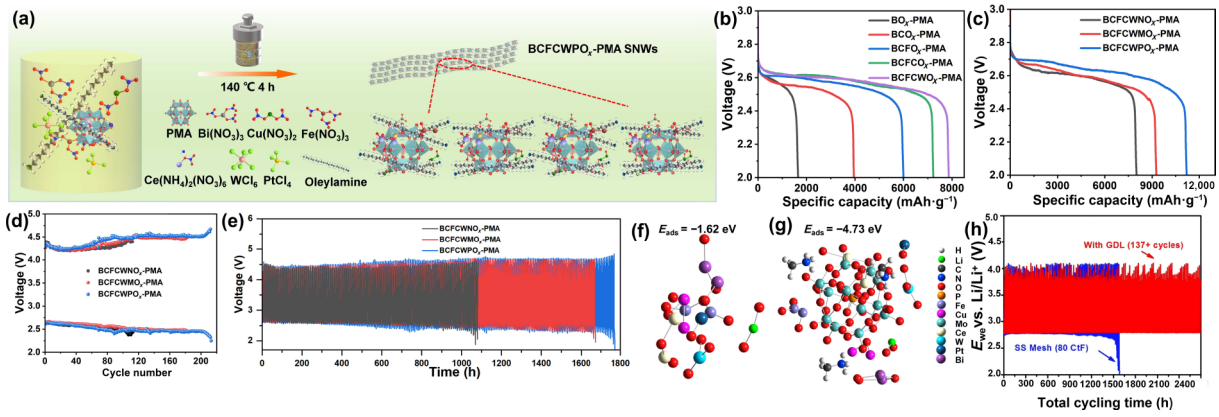


Figure 13 POM-based SNWs as cathode catalysts in LOBs. (a) Schematic diagram of the synthesized process of $BCFCWPO_x$-PMA SNWs. (b) Deep discharge curves of five kinds of POM-based SNWs at 100 mA·g^{-1}. (c) Deep discharge curves of three sorts of POM-based HEO SNWs at 100 mA·g^{-1}. (d) and (e) Cycling stability of three kinds of POM-based HEO SNWs at 100 mA·g^{-1} with a limited capacity of 500 mAh·g^{-1}. LiO_2 adsorption energy for (f) $BCFCWPO_x$ and (g) $BCFCWPO_x$-PMA SNWs. Adapted with permission from Ref. [102], © American Chemical Society 2025. (h) Cycling stability of the CNT@Ru as cathode in LOBs (GDL: carbon-based gas diffusion layers as current collector; SS: stainless steel as current collector). Adapted with permission from Ref. [181], © American Chemical Society 2016.

BCFCWPO$_x$-PMA SNWs helps improve the kinetics of the OER/ORR and thus enhance battery performance.

3.2.2 ZABs

ZABs are superior to LIBs in terms of energy density, cost-effectiveness, safety, etc. [182–184]. The discharge and charge of ZABs are four-electron processes occurring at the cathode (Fig. 12(b)) [185–187]. During the discharge reaction (ORR), the active sites on the catalyst interact with O_2 to form active oxygen atoms, which react with water to generate OH^- [101, 188]. The OER, which is the reverse of the ORR, takes place at the cathode during charge. ZAB performance is mainly limited by the slow kinetics of the OER and ORR at the cathode, which lead to a high overpotential [189–191]. Therefore, highly active cathode catalysts are required to improve ZAB performance. Although some noble metal catalysts exhibit excellent ORR/OER performance, the high cost and scarcity of noble metals limit the practical applications of ZABs. In contrast, POM-based SNMs are promising ZAB cathode catalysts because their small size and abundant surface active sites help enhance the contact between the electrode and electrolyte, shorten the distance between ions and electrons, and thereby improve the ORR/OER kinetics.

Liu et al. synthesized three types of 2D PMA-based SNSs via the CNCA strategy [107]. Under the action of Coulomb and van der Waals forces, PMA clusters interacted with various metal oxides to form 2D SNSs (Figs. 7(a)–7(c) and 14(a)–14(c)). Ultraviolet–visible absorption measurements revealed that CFNMCZ-PMA SNSs exhibited the smallest band gap (Fig. 14(d)) among the SNSs. The ability of these SNSs to promote the photoelectrochemical OER and ORR was found to be highest for CFNMCZ-PMA SNSs (Fig. 14(e)).

The voltage difference of CFNMCZ-PMA SNSs between the OER potential at 10 mA·cm^{-2} and ORR half-wave potential is only 0.591 V. Inspired by the excellent photoelectrochemical OER and ORR performances of CFNMCZ-PMA SNSs, the authors further explored the performances of the corresponding ZABs, including their power densities (Fig. 14(f)). The analysis of charge–discharge polarization curves revealed that the CFNMCZ-PMA SNS-based ZAB exhibited a higher peak power density under light (~ 102.4 mW·cm^{-2}) than that based on Pt/C + RuO_2 (~ 63.1 mW·cm^{-2}). Moreover, the former ZAB exhibited outstanding stability and could be cycled for 1600 h at 2 mA·cm^{-2} with an overpotential of 0.25 V (Fig. 14(g)). As the current density increased to 10 mA·cm^{-2}, the cycling life decreased to 930 h (Fig. 14(h)). This excellent performance was attributed to the special sub-1 nm structures exposing abundant active sites, multicomponent synergetic effect, and entropy modulation effect of POM-based HEO SNSs.

3.3 Zn symmetric batteries

Zn symmetric batteries are a type of aqueous Zn-ion batteries, which have attracted considerable attention because of their excellent electrochemical performance [192–194]. The high abundance and low mining costs of Zn reduce the cost of Zn-based batteries [195–197]. Moreover, such batteries rely on nonflammable aqueous electrolytes that are markedly safer than traditional organic systems, which greatly lowers the risks of thermal runaway, fire, and explosion [198–201]. In batteries, the separator not only separates the positive and negative electrodes to prevent short-circuiting but also facilitates ion transport. Currently reported separators suffer from several drawbacks, e.g., poor wettability, stability, and mechanical robustness [202, 203]. These issues can compromise certain battery performance metrics. Therefore, the rational design of novel separator materials is essential for further enhancing the electrochemical performance of Zn symmetric batteries.

A CS with polymer-like properties was prepared via the CNCA strategy (Fig. 15(a)) and combined with various polymers (including polyimide (PI), polyvinylpyrrolidone (PVP), polyoxyethylene (PEO), and polystyrene (PS)) to form uniform, flexible, and transparent polymer–inorganic composite films (Fig. 15(b)) [198]. More interestingly, these composite films exhibited mechanical properties superior to those of pure polymer films, which was rationalized as follows. First, when the CS diameter decreases to a sub-1 nm scale, the size effect results in properties notably different from those of macroscale inorganic materials, causing the emergence of polymer-like characteristics that facilitate the mixing of CS with polymers to form uniform composite films. Second, the sub-1 nm size endows CS with a high aspect ratio and surface atom exposure rate, which promotes CS–polymer contact and thus helps resist external forces. Most importantly, the oxygen-rich POM surface enables noncovalent interactions with polymers, which enhances the flexibility of the composite film. CS–PI films with different contents of mass were

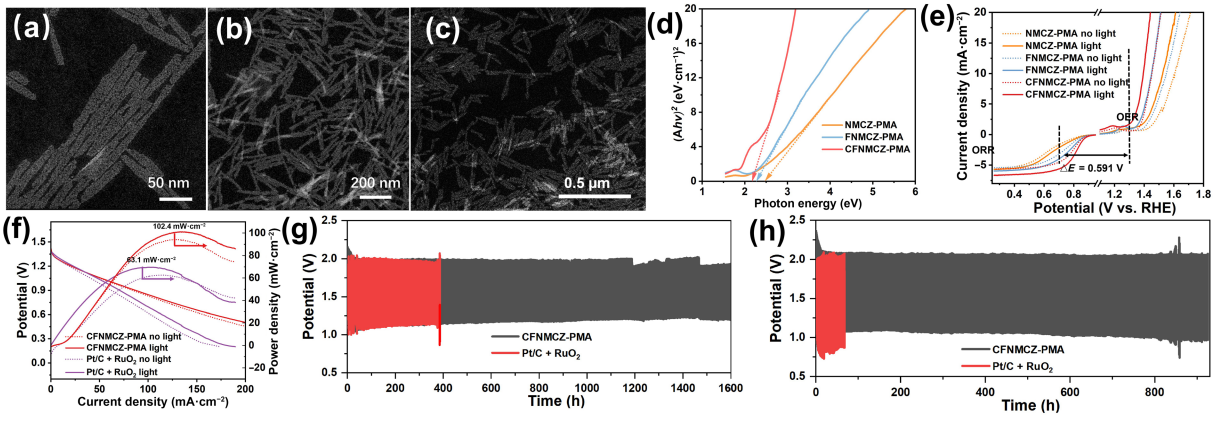


Figure 14 POM-based SNSs as the cathode catalysts in light-assisted ZABs. (a)–(c) HAADF-STEM images of NMCZ-PMA SNSs, FNMCZ-PMA SNSs, and CFNMCZ-PMA SNSs. (d) The Tauc plots of NMCZ-PMA, FNMZC-PMA, and CFNMZC-PMA SNSs derived from UV–vis absorption spectra. (e) Polarization curves of ORR and OER. (f) Discharge polarization curves and the corresponding power density–current density curves of the CFNMCZ-PMA SNSs and Pt/C + RuO_2-based ZABs with/without light. Potential vs. time curves of the rechargeable CFNMCZ-PMA SNSs and Pt/C + RuO_2-based ZABs at (g) 2 and (h) 10 mA·cm^{-2}. Adapted with permission from Ref. [107], © American Chemical Society 2024 .

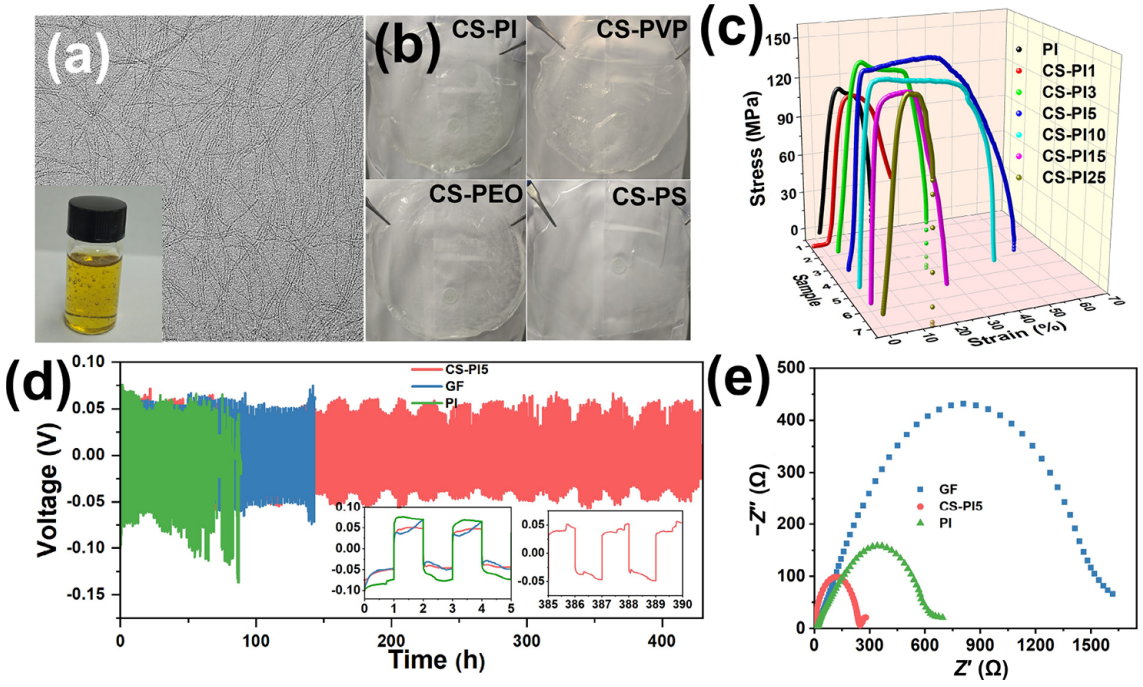


Figure 15 The polymer-inorganic composite films as the separator in Zn symmetric batteries. (a) The TEM image of Ce_2O_3-PMA SNWs (CS) (the inset is the optical photograph of CS dispersion liquid, where bubbles trapped in the dispersion liquid after shaking for a long time). (b) The optical photographs of the CS-PI film, CS-PVP film, CS-PEO film, and CS-PS film. (c) The stress–strain curves of PI and CS-PI films. (d) Cycle performance of the Zn symmetric battery with the glass fiber (GF), PI, and CS-PI5 film as the separator at 1 mA·cm^{-2} for 1 mAh·cm^{-2} (the insets show magnified images at different cycle time). (e) Nyquist plots of Zn symmetric cells with the three films as the separator before cycling. Adapted with permission from Ref. [198], © Wiley-VCH GmbH 2025.

prepared and examined in terms of their mechanical properties (Fig. 15(c)). Subsequently, the film with the best mechanical properties (CS-PI5) was used as a separator in Zn symmetric batteries. The high aspect ratio of CS enables its efficient interaction with PI to provide a fast transport interface for Zn ions. Unlike those with a commercial separator and pure PI film, the battery with the CS-PI5 film could be stably cycled 430 h (Fig. 15(d)). Electrochemical impedance spectroscopy (EIS) measurements (Fig. 15(e)) showed that the CS-PI5 film separator results in a lower charge transfer resistance (R_{ct}) than GF and PI films and can therefore improve the interfacial kinetics of batteries. Moreover, the CS-PI5 film enabled the fastest Zn plating/stripping. This work suggests that POM-based SNMs can be used not only as electrode materials but also as separator materials, thus providing insights into the design of novel separator materials and expanding the application scope of POM-based SNMs.

3.4 LSBs

Most commercial LIBs struggle to exceed the theoretical energy density of ~ 350 Wh·kg^{-1} [204–206]. In contrast, LSBs show great development potential, as their theoretical energy density (2567 Wh·kg^{-1}) far surpasses that of LIBs [207, 208]. Additionally, the corresponding electrode material (S) is extremely abundant in Earth's crust, cheap, ecofriendly, and possesses excellent sustainability and economic viability [209–211]. However, polysulfide shuttling, sluggish polysulfide conversion kinetics, and Li dendrite formation lead to poor stability and thus hinder commercialization [212–217]. Although polymer films are widely used as separators in batteries, the weak interactions between polymers and polysulfides and poor battery performance of polymers result in noncompliance with LSB requirements. Fortunately, POM-based SNWs with polymer-like properties can be processed into films that can be used as separators to enhance LSB performance [218].

Wang et al. prepared Bi_2O_3-POM SNWs (PMB SNWs) with polymer-like properties (Fig. 16(a)). Then, polymer-resembling films with superaligned PMB SNWs (S-PMB SNWs) were prepared by a wet-spinning method and used as LSB separators [218]. In the battery reaction, the oxygen-rich POM surface can be regarded as a Lewis acid, whereas polysulfides act as Lewis bases. When polysulfides are adsorbed on S-PMB SNWs, electrons are transferred from the polysulfides to the Mo atoms of POMs. This adsorption suppresses polysulfide shuttling, thereby accelerating the battery reaction. Experimental and theoretical evidence indicate that polysulfide shuttling is synergistically impeded by all constituents of PMB NWs. EIS measurements (Fig. 16(b)) indicate that compared with a polypropylene (PP) film, the S-PMB SNW film exhibits lower impedance and forms a thinner insulating layer. Moreover, compared with PP film-based LSBs, the S-PMB SNW film-based LSBs showed better rate performance, higher capacities at different current densities, and a greater stability. At 2 C, the S-PMB SNW film-based LSBs could be operated for 850 cycles with a specific capacity of 782 mAh·g^{-1} and only 0.013% capacity fading per cycle (Fig. 16(c)), outperforming their counterparts based on other nanoparticles (Fig. 16(d)) [219]. This work indicates that owing to their sub-1 nm structure and combination of effective components, S-PMB SNW films can prevent Li polysulfide shuttling, accelerate LI polysulfide conversion, and protect the Li anode.

4 Applications of POM-based SNMs in energy conversion

The efficient conversion of solar energy into various energy forms needed in daily life is strategically important because of its wide

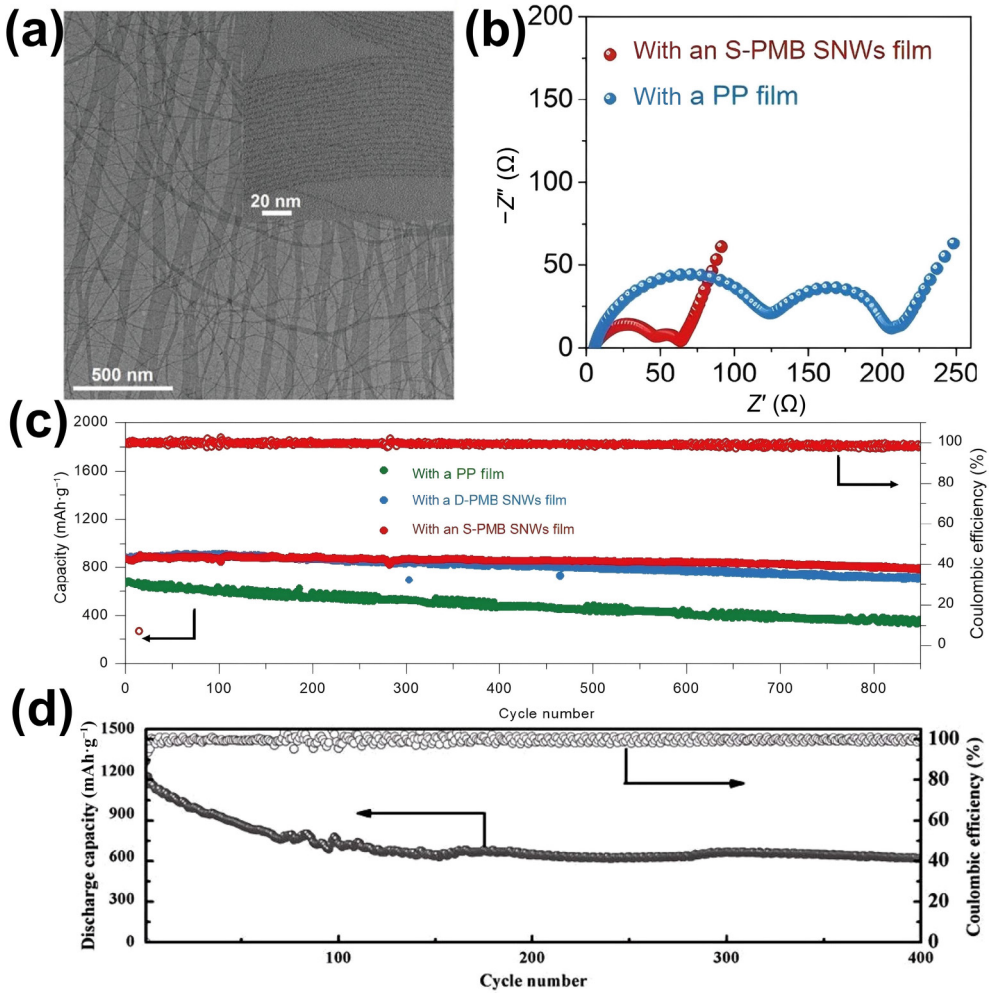


Figure 16 The S-PMB SNWs film as the separator in LSBs. (a) TEM image of the PMB SNWs. (b) Nyquist plots of LSBs with a PP film and S-PMB SNWs film, respectively. (c) Cyclic performance of LSBs with three kinds of films as the separator at 2 C. Adapted with permission from Ref. [218], © Science China Press and Springer-Verlag GmbH Germany, part of Springer Nature 2021. (d) Cycling performance of the LSB assembled with PIE (PIE: the electrode prepared by phase inversion method). Adapted with permission from Ref. [219], © WILEY-VCH Verlag GmbH & Co. KGaA, Weinheim 2016.

distribution, infinite reserves, and ecofriendly nature [220–222]. POM-based SNMs exhibit promising application prospects in this field [95, 99, 101]. SNMs typically exhibit high atomic exposure and hence, abundant free electrons. This property enhances the surface plasmon resonance effect, thereby notably improving light absorption capability. SNMs can effectively capture solar energy and convert it into thermal energy, which can then be applied in photothermal conversion, solar steam generation, and seawater desalination, providing a new technical direction for solving the problem of freshwater scarcity.

Based on the CNCA strategy, Wang et al. synthesized POM-based SNMs with outstanding photothermal conversion properties, including MoO_3-POM HSNSs [99], CuO-PMA SNSs [95], and Bi_2O_3-PMoO SNWs [218]. The four types of MoO_3-POM HSNSs exhibited strong absorption in the ultraviolet to near-infrared region and could therefore possess certain photothermal conversion properties (Fig. 17(a)). Under irradiation with an 808 nm laser at 1 W·cm^{-2}, the temperature of the MoO_3-POM HSNSs increased by ~ 40 °C, with the highest photothermal conversion efficiency observed for MoO_3-$PW_{12}O_{40}$ HSNSs (Fig. 17(b)) [99]. The 2D CuO-PMA SNSs also exhibit strong absorption in the ultraviolet to near-infrared region [95]. Under irradiation with an 808 nm laser at 1 W·cm^{-2}, these SNSs experienced a temperature increase of 31.9 °C, as recorded by an infrared camera at different times (Fig. 17(c)). When the light intensity was increased to 2 W·cm^{-2}, the temperature increased by 50 °C (Fig. 17(d)). The photothermal conversion performance was superior to that of previously reported Cu-based nanomaterials, which was attributed to the synergistic effect of CuO and PMA, as well as the surface electronic resonance of the SNMs. In addition, CuO-PMA SNSs could be fabricated into films for solar steam generation. Under 1 sun illumination, the CuO-PMA SNS membrane delivered a water evaporation rate of 1.41 kg·m^{-2}·h^{-1} and an energy conversion efficiency of 95.72%, corresponding to 3.4 times that of bulk water (Fig. 17(e)). The membrane exhibited excellent stability and could be recycled at least 10 times without a notable decline in performance (Fig. 17(f)). More importantly, the CuO-PMA SNS membrane could be used for seawater desalination, delivering an evaporation rate of 1.325 kg·m^{-2}·h^{-1} in simulated seawater under 1 sun (Fig. 17(g)). After evaporation, the concentrations of four primary ions (Na^+, Mg^{2+}, K^+, and Ca^{2+}) in the collected water were 3–4 orders of magnitude lower than those in the original seawater (Fig. 17(h)). The above progress suggests that POM-based SNMs show potential advantages for energy conversion, especially

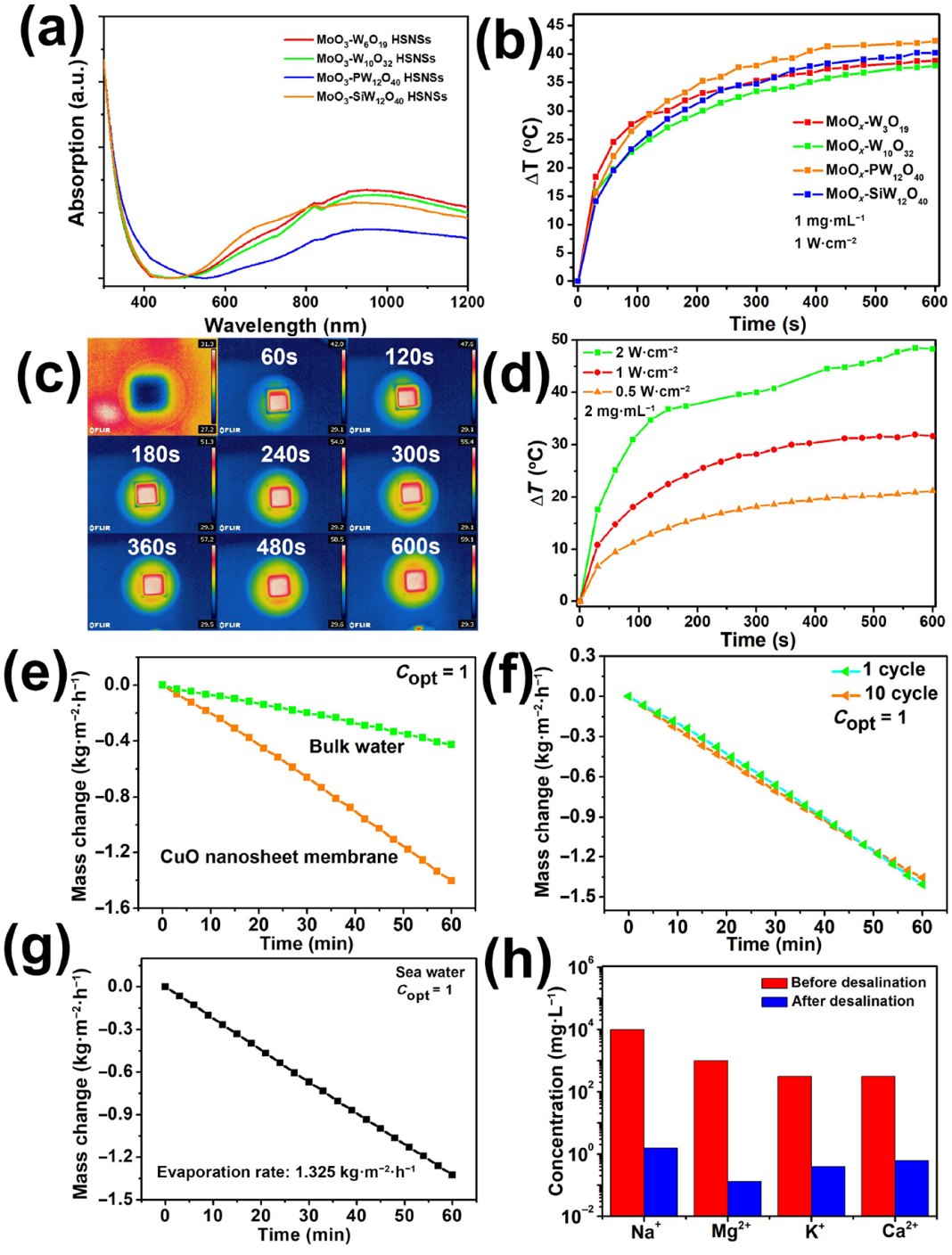


Figure 17 POM-based SNMs applied in energy conversion. (a) The UV–vis absorption spectra of four kinds of MoO_3-POM HSNSs. (b) Temperature changes of four types of MoO_3-POM HSNSs dispersion (1 mg·mL^{-1}) under 1 W·cm^{-2}. Adapted with permission from Ref. [99], © American Chemical Society 2020. (c) Time-dependent photothermal images of CuO-PMA SNSs captured by an infrared camera. (d) Temperature evolution of CuO-PMA SNSs (2 mg·mL^{-1}) with irradiation time under 808 nm laser irradiation (power densities: 0.5, 1, and 2 W·cm^{-2}). (e) Mass changes of bulk water versus water covered with the CuO-PMA SNSs membrane under 1 sun irradiation. (f) Mass changes of the CuO-PMA SNSs membrane in the 1st and 10th cycle during stability test under 1 sun illumination. (g) The mass change of seawater covered with the CuO-PMA SNSs membrane under 1 sun illumination. (h) The concentration of Na^+, Mg^{2+}, K^+, and Ca^{2+} in seawater before and after desalination. Adapted with permission from Ref. [95], © American Chemical Society 2019.

seawater desalination.

5 Conclusions and perspectives

This review summarizes the methods of synthesizing POM-based SNMs and their applications in energy storage and photothermal conversion. POM-based SNMs have many advantages over large-sized materials, as exemplified by the ability of the former to accelerate the reactions responsible for battery charge–discharge and thereby improve specific discharge capacity and cycling stability. In photothermal conversion applications, POM-based SNMs can achieve a high temperature rise within a short period,

thus holding promise for solar steam evaporation and seawater desalination. Despite these advantages, POM-based SNMs face certain challenges, which can potentially be addressed as follows.

(1) Explore more synthesis methods. Hydrothermal/solvothermal synthesis is currently the main method of preparing POM-based SNMs. Under hydrothermal/solvothermal conditions, POM-based SNMs can be synthesized based on the CNCA strategy, which has shown certain advantages. However, the application scope of this strategy should be expanded by, e.g., replacing POM clusters with other kinds of metal clusters of sub-1 nm size. Additionally, more synthetic methods should be explored to develop efficient, low-risk, low-cost, and ecofriendly procedures. Current methods can only produce milligrams of SNMs at a time, whereas application scope expansion requires gram- or kilogram-scale production.

(2) Expand the scope of POM-based SNMs. Currently, most POM-based SNMs prepared via the CNCA strategy are metal oxides. Efforts should be devoted to synthesizing different kinds of SNMs (such as sulfides, tellurides, and selenides) and thereby expanding the practical application scope of POM-based SNMs.

(3) The formation mechanism of POM-based SNMs needs to be further investigated. MD simulations used to explore the formation mechanism of POM-based SNMs mainly revealed that under the action of noncovalent forces, POMs coassemble with sub-1 nm nuclei to form cluster–nuclei coassemblies, which grow into different kinds of SNMs. However, at the current stage, we cannot explain how to precisely control material morphology and dimensions at the sub-1 nm scale.

(4) Expand the application range of POM-based SNMs. POM-based SNMs have been used in photothermal conversion, LIBs, SIBs, LOBs, ZABs, etc. However, the corresponding systems have not been widely applied. Therefore, researchers need to design and synthesize POM-based SNMs with higher energy conversion efficiencies, higher specific discharge capacities, and longer lifetimes to promote the practical applications of these materials, such as seawater desalination and new energy vehicles.

In conclusion, owing to the size effect, POM-based SNMs have a large specific surface area and numerous exposed active sites, thus outperforming large-sized materials in several aspects and enabling notable progress in energy storage and conversion. However, researchers still need to explore more efficient, low-cost, and ecofriendly methods to synthesize POM-based SNMs at a greater scale. We believe that with more researchers joining this field in the future, progress in POM-based SNMs is inevitable.

Data availability

Not applicable.

Acknowledgements

J. L. L. is thankful for the support from the National Natural Science Foundation of China (No. 22305012), the Fundamental Research Funds for the Central Universities and the Xiaomi Young Talents Program. Y. Z. is thankful for the support from the National Key Research and Development Program of China (No. 2024YFA1211101), the National Natural Science Foundation of China (Nos. 52432004 and U22A20141), and the Research Funding of Hangzhou International Innovation Institute of Beihang University (Nos. 2024KQ102 and 2024KQ131).

Declaration of competing interest

The authors have no competing interests to declare that are relevant to the content of this article.

Author contribution statement

The review was written through contributions of all authors. All authors have given approval to the final version of the manuscript.

Use of AI statement

None.

References

[1] Kumar, R.; Kumar, D.; Lokhande, P. E.; Kadam, V.; Jagtap, C.; Vedapathak, A. S.; Singh, K.; Mishra, Y. K.; Kaushik, A. Emergence of perovskites oxides as advanced Photocatalysts for energy and environmental remediation applications. *Coord. Chem. Rev.* **2025**, *534*, 216556.

[2] Meng, S. Y.; Lu, Y. Superwettable nanomaterials: Fabrication, application, and environmental impact. *ACS Nano* **2025**, *19*, 7417–7433.

[3] Kahia, M.; Aïssa, M. S. B.; Lanouar, C. Renewable and non-renewable energy use-economic growth nexus: The case of MENA net oil importing countries. *Renew. Sustain. Energy Rev.* **2017**, *71*, 127–140.

[4] Somoye, O. A. Energy crisis and renewable energy potentials in Nigeria: A review. *Renew. Sustain. Energy Rev.* **2023**, *188*, 113794.

[5] Valadkhani, A.; Nguyen, J. Long-run effects of disaggregated renewable and non-renewable energy consumption on real output. *Appl. Energy* **2019**, *255*, 113796.

[6] Cheng, D. Y. Solar and wind. *Nat. Climate Change* **2023**, *13*, 1020.

[7] Blaabjerg, F.; Ma, K. Wind energy systems. *Proc. IEEE* **2017**, *105*, 2116–2131.

[8] Boettcher, S. W. Introduction to green hydrogen. *Chem. Rev.* **2024**, *124*, 13095–13098.

[9] Sleiti, A. K. Tidal power technology review with potential applications in Gulf Stream. *Renew. Sustain. Energy Rev.* **2017**, *69*, 435–441.

[10] Amal, R.; Zhao, H. J.; Wang, D.; Wang, L. Z. Renewable energy conversion and storage. *Adv. Energy Mater.* **2017**, *7*, 1703091.

[11] Mperejekumana, P.; Shen, L.; Zhong, S.; Gaballah, M. S.; Muhirwa, F. Exploring the potential of decentralized renewable energy conversion systems on water, energy, and food security in Africa. *Energy Convers. Manage.* **2024**, *315*, 118757.

[12] Qi, J.; Zhang, W.; Cao, R. Solar-to-hydrogen energy conversion based on water splitting. *Adv. Energy Mater.* **2018**, *8*, 1701620.

[13] Zhao, X.; Nashalian, A.; Ock, I. W.; Popoli, S.; Xu, J.; Yin, J. Y.; Tat, T.; Libanori, A.; Chen, G. R.; Zhou, Y. H. et al. A soft magnetoelastic generator for wind-energy harvesting. *Adv. Mater.* **2022**, *34*, 2204238.

[14] Ager, J. W.; Lapkin, A. A. Chemical storage of renewable energy. *Science* **2018**, *360*, 707–708.

[15] Durmus, Y. E.; Zhang, H.; Baakes, F.; Desmaizieres, G.; Hayun, H.; Yang, L. T.; Kolek, M.; Küpers, V.; Janek, J.; Mandler, D. et al. Side by side battery technologies with lithium-ion based batteries. *Adv. Energy Mater.* **2020**, *10*, 2000089.

[16] Jiang, L. W.; Lu, Y. X.; Zhao, C. L.; Liu, L. L.; Zhang, J. N.; Zhang, Q. Q.; Shen, X.; Zhao, J. M.; Yu, X. Q.; Li, H. et al. Building aqueous K-ion batteries for energy storage. *Nat. Energy* **2019**, *4*, 495–503.

[17] Lin, C. K.; Wang, J. X.; He, H. J.; Liu, X. T.; Qiu, F. L.; Jin, Q. W.; Li, H.; Sun, Y.; Li, S.; Zhang, Y. et al. Self-charged dual-

photoelectrode vanadium-iron energy storage battery. *Adv. Energy Mater.* **2024**, *14*, 2303126.
[18] Song, K.; Agyeman, D. A.; Park, M.; Yang, J.; Kang, Y. M. High-energy-density metal-oxygen batteries: Lithium-oxygen batteries vs sodium-oxygen batteries. *Adv. Mater.* **2017**, *29*, 1606572.
[19] Chang, W. C.; Wu, J. H.; Chen, K. T.; Tuan, H. Y. Red phosphorus potassium-ion battery anodes. *Adv. Sci.* **2019**, *6*, 1801354.
[20] Huang, H. J.; Wu, X. W.; Gao, Y. J.; Li, Z. Y.; Wang, W.; Dong, W. S.; Song, Q. Y.; Gan, S. J.; Zhang, J. G.; Yu, Q. Y. Polyanionic cathode materials: A comparison between Na-ion and K-ion batteries. *Adv. Energy Mater.* **2024**, *14*, 2304251.
[21] Mao, Z. F.; Wang, H. W.; Zhang, T. Q.; Wang, Y. F.; Zhou, W. H.; Chao, D. L. Synergetic electrolyte chemistry enables flame-retardancy, K^+-desolvation, anti-corrosion and wide-temperature-tolerance in potassium-ion batteries. *J. Am. Chem. Soc.* **2025**, *147*, 34059–34069.
[22] Ji, B. F.; Zhang, F.; Song, X. H.; Tang, Y. B. A novel potassium-ion-based dual-ion battery. *Adv. Mater.* **2017**, *29*, 1700519.
[23] Cai, Y. C.; Hou, Y. P.; Lu, Y.; Zhang, Q.; Yan, Z. H.; Chen, J. Ionic liquid electrolyte with weak solvating molecule regulation for stable Li deposition in high-performance Li–O_2 batteries. *Angew. Chem., Int. Ed.* **2023**, *62*, e202218014.
[24] Song, L. N.; Liang, S.; Wang, Y.; Du, X. Y.; Sun, Y.; Yuan, X. Y.; Wang, H. F.; Xu, J. J. Record-breaking discharge capacity and rate capability in Li–O_2 batteries through magnetic field-induced short-range order Li_2O_2. *Angew. Chem., Int. Ed.* **2025**, *64*, e20097.
[25] Wang, M.; Tian, Z. L.; Li, G. X.; Xiao, Y. K.; Chen, G. W.; Li, S. Y.; Su, R. Q.; Cui, B. H.; Jiang, C. L.; Sun, Z. J. et al. Edge-dislocated WO_3 photocathode toward efficient photo-assisted Li–O_2 batteries. *Adv. Mater.* **2025**, *37*, e01716.
[26] Hao, Q. Q.; Cai, Z. P.; Zhao, X. H.; Wang, L. Y.; Wang, K. X.; Chen, J. S. Boosting the efficiency and stability of Li–CO_2 batteries via a ruthenium-based olefin-metathesis catalyst. *J. Am. Chem. Soc.* **2024**, *146*, 27802–27808.
[27] Li, J. T.; Liu, L. M.; Guan, D. H.; Liang, H.; Lu, Z. C.; Wang, H.; Zhang, Y. W.; Tang, J. M.; Chen, S. H.; Feng, G. D. et al. *d-p* orbital hybridization tailoring for boosted redox kinetics in Li–CO_2 batteries. *Adv. Funct. Mater.* **2026**, *36*, e14223.
[28] Pan, Q.; Yang, L.; Wang, H. J.; Liu, H. X.; Shu, Y. M.; Li, L.; Yang, S.; Zhang, W. Y.; Mao, Y.; Xie, J. Y. et al. Interfacial thiophilicity enrichment for efficient Li–CO_2 batteries. *Adv. Funct. Mater.*, in press, DOI: 10.1002/adfm.202522446.
[29] Li, J. Y.; Du, X. Y.; Wang, X. X.; Yuan, X. Y.; Guan, D. H.; Xu, J. J. Photo-assisted Li–N_2 batteries with enhanced nitrogen fixation and energy conversion. *Angew. Chem., Int. Ed.* **2024**, *63*, e202319211.
[30] Meng, F. B.; Qin, J. Y.; Xiong, X. Y.; Li, X. J.; Hu, R. Z. Understanding the reversible reactions of Li–N_2 battery catalyzed with SnO_2. *Energy Environ. Mater.* **2023**, *6*, e12298.
[31] Zhang, Z.; Wu, S. S.; Yang, C.; Zheng, L. Y.; Xu, D. L.; Zha, R. H.; Tang, L.; Cao, K. Z.; Wang, X. G.; Zhou, Z. Li–N_2 batteries: A reversible energy storage system? *Angew. Chem., Int. Ed.* **2019**, *58*, 17782–17787.
[32] Gu, T. T.; Zhang, C. H.; Xi, L.; Ouyang, L. Z.; Zhu, M.; Liu, J. High-entropy electrocatalytic materials in Zn-air batteries: From fundamentals to applications. *Adv. Mater.* **2026**, *38*, e12274.
[33] Li, L. F.; Liu, Y. X.; Zhang, X.; Humayun, M.; Yang, H. W.; Zeng, J. R.; Younus, H. A.; Pang, Y. J.; Wang, D. L.; Snyders, R. et al. Curvature strain-induced electron spin leveraging in d orbitals toward oxygen reduction for Zn-air batteries. *Nano Lett.* **2025**, *25*, 16459–16467.
[34] Zhang, Q. W.; Wang, J.; Yang, W. H.; Du, X. F.; Zhao, J. W.; Wang, J. Z.; Lu, G. L.; Chen, Z.; Ge, X. S.; Xiao, J. et al. Rechargeable aprotic zinc-oxygen batteries with reversible ZnO formation on cathodes. *Angew. Chem., Int. Ed.* **2026**, *65*, e19306.
[35] Rao, Y.; Yang, J. W.; Chu, S. Y.; Guo, S. H.; Zhou, H. S. Solid-state Li-air batteries: Fundamentals, challenges, and strategies. *SmartMat* **2023**, *4*, e1205.
[36] Wang, Z. R.; Ni, Z. W.; Chen, J.; Dai, Y. M.; Gao, Y. S.; Zhang, Q.; Dong, F. B.; Xiong, S. L.; Zhang, C. H.; Feng, J. K. Recent progress and challenges on emerging high-entropy materials for better Zn-Air and Zn-Ion batteries. *Energy Storage Mater.* **2025**, *75*, 104064.
[37] Yang, C. B.; Singh, A.; Pu, X. F.; Mallarapu, A.; Smith, K.; Keyser, M.; Haberman, M. R.; Khani, H.; Misztal, P.; Spray, R. et al. Addressing the safety of next-generation batteries. *Nature* **2025**, *645*, 603–613.
[38] Zhao, L. N.; Zhang, T.; Li, W.; Li, T.; Zhang, L.; Zhang, X. G.; Wang, Z. Y. Engineering of sodium-ion batteries: Opportunities and challenges. *Engineering* **2023**, *24*, 172–183.
[39] Gu, Y. D.; Zhao, E. D.; Wan, X. Y.; Ma, J.; Liu, D.; Xiong, Y. J. Reaction-induced phase engineering of CuCo nanoparticles for enhanced photothermal CO_2 hydrogenation. *Adv. Mater.*, in press, DOI: 10.1002/adma.202515661.
[40] Guo, L. Z.; Wu, L. B.; Jia, T.; Zhang, H. T.; Song, J. L.; Xie, X. Q.; Jee, M. H.; Ma, H. S.; Liu, S.; Lu, G. H. et al. Aggregation-enhanced-emission polymer donor improves the efficiency of organic solar cells by suppressing nonradiative recombination. *Angew. Chem., Int. Ed.* **2025**, *64*, e202516421.
[41] Li, J. L.; Zhao, J. W.; Wang, S. B.; Peng, K. S.; Su, B.; Liu, K. L.; Hung, S. F.; Huang, M. R.; Zhang, G. G.; Zhang, H. B. et al. Activating lattice oxygen in perovskite ferrite for efficient and stable photothermal dry reforming of methane. *J. Am. Chem. Soc.* **2025**, *147*, 14705–14714.
[42] Sachs, M.; Harnett-Caulfield, L.; Pastor, E.; Davies, B.; Sowood, D. J. C.; Moss, B.; Kafizas, A.; Nelson, J.; Walsh, A.; Durrant, J. R. Metal-centred states control carrier lifetimes in transition metal oxide photocatalysts. *Nat. Chem.* **2025**, *17*, 1348–1355.
[43] Cao, Y. H.; Wang, J. M.; Guan, W. X.; An, M.; Yan, P.; Li, Z. T.; Zhao, C. S.; Yu, G. H. Spatially regulated water-heat transport by fluidic diode membrane for efficient solar-powered desalination and electricity generation. *Nat. Commun.* **2025**, *16*, 5050.
[44] Li, N.; Zou, Y.; Zhang, X. Q.; Jin, Z. K.; Yang, Y.; Yang, L.; Duan, G. G.; Xu, Y. T.; Li, Y. W. Degradable and recyclable solar desalination membranes based on naturally occurring building blocks. *Chem. Mater.* **2022**, *34*, 10399–10408.
[45] Liang, C. G.; Yasin, A.; Zhang, L. S.; Zhang, P.; Zhou, K. F.; Hao, B.; Li, H.; Ma, P. C. Solar interfacial evaporator with three-dimensional architecture for seawater desalination. *Colloids Surf. A: Physicochem. Eng. Aspects* **2024**, *702*, 135035.
[46] Zhu, J.; Qiu, S. E.; Duan, M. Y.; Xie, Q. H.; Jiang, O. S.; Zhao, X. R.; Wu, D.; Liu, Y. X.; Chen, G.; Huang, X. Y. et al. Polyelectrolyte gradient hydrogels for efficient solar evaporation. *Adv. Funct. Mater.* **2026**, *36*, e12350.
[47] Chen, S. Q.; Zhu, Y. X.; Xu, Q. Q.; Jiang, Q.; Chen, D. Y.; Chen, T.; Xu, X. S.; Jin, Z. K.; He, Q. J. Photocatalytic glucose depletion and hydrogen generation for diabetic wound healing. *Nat. Commun.* **2022**, *13*, 5684.
[48] Sun, J. Q.; Feng, Y. M.; Zheng, R.; Mao, Y. M.; Zhu, Q. L.; Wu, X. G.; Kong, L. R.; Zhang, K.; Liu, S. T. Solar-enhanced low-temperature biological wastewater treatment. *Nat. Sustain.* **2025**, *8*, 1048–1057.
[49] Niu, M. T.; Li, Q. R.; Huang, Q. X.; Qin, Y. T.; Meng, D.; Liang, J. L.; Zhang, X. Z. Amplifying synergistic effects of cuproptosis and bacterial membrane vesicles-mediated photothermal therapy by multifunctional nano-biohybrid for anti-tumor immunotherapy. *Adv. Funct. Mater.* **2025**, *35*, 2413255.
[50] Wang, J.; Zhang, J. H.; Li, Y.; Xia, X. H.; Yang, H. J.; Kim, J. H.; Zhang, W. Silver single atoms and nanoparticles on floatable monolithic photocatalysts for synergistic solar water disinfection. *Nat. Commun.* **2025**, *16*, 981.
[51] Xiu, W. J.; Wan, L.; Yang, K. L.; Li, X.; Yuwen, L. H.; Dong, H.; Mou, Y. B.; Yang, D. L.; Wang, L. H. Potentiating hypoxic microenvironment for antibiotic activation by photodynamic therapy

to combat bacterial biofilm infections. *Nat. Commun.* **2022**, *13*, 3875.
[52] Cheng, Y.; Qin, K. J.; Zang, D. J. Polyoxometalates based nanocomposites for bioapplications. *Rare Met.* **2023**, *42*, 3570–3600.
[53] Song, W. T.; Song, B.; Liang, Y. H.; Zhou, Y.; Wang, B.; Gao, W. G.; Wu, Y.; Ling, X.; Liu, Y.; Ye, R. Q. et al. Precise dual-metal pairs enable ultrafast structural response for CO_2-to-ethylene photoconversion. *J. Am. Chem. Soc.* **2025**, *147*, 39505–39515.
[54] Zhao, Z. C.; Wei, J. Y.; Lang, Z. L.; Chi, M. Z.; Liu, X. Y.; Yang, J. X.; Yang, G. Y.; Lv, H. J. A Superatomic $\{Ag_8\}^{6+}$ cluster induced by asymmetric mixed-addendum polyoxometalate. *J. Am. Chem. Soc.* **2025**, *147*, 25107–25114.
[55] Zhou, Z. B.; Wang, Z. T.; Blenko, A. L.; Li, J. H.; Lin, W. B. Viologen covalent organic framework mediates near-infrared light-induced electron transfer for catalytic oxidative coupling reactions. *J. Am. Chem. Soc.* **2025**, *147*, 10846–10852.
[56] Bao, T.; Tang, C. C.; Wu, Y. N.; Bi, Y.; Zhang, C. Q.; Xi, Y. M.; Zou, Y. Y.; Liu, C.; Yu, C. Z. Photocatalytic Co-reduction of CO_2 and nitrate over porphyrin metal-organic frameworks: Dual atomic active site and nanostructure synergy enhances C–N coupling for urea production. *Angew. Chem., Int. Ed.* **2025**, *64*, e202512615.
[57] Kang, L. L.; Zhu, B. E.; Gu, Q. Q.; Duan, X. Y.; Ying, L.; Qi, G. D.; Xu, J.; Li, L.; Su, Y.; Xing, Y. N. et al. Light-driven propane dehydrogenation by a single-atom catalyst under near-ambient conditions. *Nat. Chem.* **2025**, *17*, 890–896.
[58] Rao, Z. Q.; Huang, Z. A.; Zhang, K. K.; Wang, J. B.; Feng, Y. B.; Wang, K. W.; Chen, Y. L.; Cao, Y. H.; Li, L. N.; Jiang, A. Q. et al. Concentrated-solar catalytic methane dry reforming with ultrahigh conversion and durability. *Nat. Commun.* **2025**, *16*, 9605.
[59] Liu, J. L.; Nie, S. Y.; Wu, L.; Wang, X. High-entropy metal oxide-polyoxometalate-palladium sub-1 nm nanowires for semi-hydrogenation reaction of alkynes. *Chem. Res. Chin. Univ.* **2023**, *39*, 624–629.
[60] Liu, J. L.; Wang, S. B.; Liu, N.; Yang, D. R.; Wang, H. W.; Hu, H. S.; Zhuang, J.; Wang, X. Au-polyoxometalates A-B-A-B type copolymer-analogue sub-1 nm nanowires. *Small* **2021**, *17*, 2006260.
[61] Ni, B.; Shi, Y. A.; Wang, X. The sub-nanometer scale as a new focus in nanoscience. *Adv. Mater.* **2018**, *30*, 1802031.
[62] Liu, J. L.; Li, Y. Q.; Chen, Z.; Liu, N.; Zheng, L. R.; Shi, W. X.; Wang, X. Polyoxometalate cluster-incorporated high entropy oxide sub-1 nm nanowires. *J. Am. Chem. Soc.* **2022**, *144*, 23191–23197.
[63] Liu, Q. D.; Sheng, Z.; Shi, W. X.; Cheng, X. J.; Xu, X. X.; Wang, X. Tuning the chirality evolution in achiral subnanometer systems by judicious control of molecule interactions. *J. Am. Chem. Soc.* **2024**, *146*, 12819–12827.
[64] Zhang, S. M.; Shi, W. X.; Wang, X. Locking volatile organic molecules by subnanometer inorganic nanowire-based organogels. *Science* **2022**, *377*, 100–104.
[65] Zhang, S. M.; Wang, X. Inorganic subnanometer nanowire-based organogels: Trends, challenges, and opportunities. *ACS Nano* **2023**, *17*, 20–26.
[66] Liu, J. L.; Wang, M. X.; Dipalo, M. C.; Zhuang, J.; Shi, W. X.; Wang, X. Ternary hybrid CuO-PMA-Ag sub-1 nm nanosheet heterostructures. *Chem. Sci.* **2021**, *12*, 11490–11494.
[67] Liu, J. L.; Zhuang, J.; Shi, W. X.; Wang, X. $Ni(OH)_2$-polyoxometalate cluster hybrid superstructures. *Chem. Mater.* **2021**, *33*, 7100–7105.
[68] Zang, D. J.; Gao, X. J.; Li, L. Y.; Wei, Y. G.; Wang, H. Q. Confined interface engineering of self-supported Cu@N-doped graphene for electrocatalytic CO_2 reduction with enhanced selectivity towards ethanol. *Nano Res.* **2022**, *15*, 8872–8879.
[69] Zang, D. J.; Li, Q.; Dai, G. Y.; Zeng, M. Y.; Huang, Y. C.; Wei, Y. G. Interface engineering of Mo_8/Cu heterostructures toward highly selective electrochemical reduction of carbon dioxide into acetate. *Appl. Catal. B: Environ.* **2021**, *281*, 119426.
[70] Xu, S. Y.; Wang, P.; Zhang, B. W.; Wang, C.; Low, J.; Ivanov, V. K.; Zhang, Z. M. Nickel-substituted polyoxometalate-CdS single-cluster photocatalysts for efficient plastic waste degradation coupled with H_2 production. *Polyoxometalates* **2025**, *4*, 9140096.
[71] Wang, Z. R.; Ye, Q. H.; Chen, W. C.; Zhao, Y. L.; Cao, X. J.; Shi, W. X.; He, P. L. Electronic structure engineering of sub-1 nm $Ni(OH)_2$ nanowires through Fe incorporation in polyoxometalates for superior water oxidation. *Adv. Funct. Mater.* **2026**, *36*, e11187.
[72] Yuan, G. B.; Liu, J. L.; Zhang, Y. Sub-1 nm nanomaterials applied in energy storage. *Batter. Storage.* **2024**, *7*, e202300623.
[73] Liu, Q. D.; Wang, X. Polyoxometalate clusters: Sub-nanometer building blocks for construction of advanced materials. *Matter* **2020**, *2*, 816–841.
[74] Liu, Q. D.; Wang, X. Cluster-assembled materials: Ordered structures with advanced properties. *InfoMat* **2021**, *3*, 854–868.
[75] Liu, Q. D.; Wang, X. Sub-nanometric materials: Electron transfer, delocalization, and beyond. *Chem Catal.* **2022**, *2*, 1257–1266.
[76] Liu, Q. D.; Wang, X. Fabricating sub-nanometer materials through cluster assembly. *Chem. Sci.* **2022**, *13*, 12280–12289.
[77] Liu, Q. D.; Wang, X. Precise assembly of polyoxometalates at single-cluster levels. *Angew. Chem., Int. Ed.* **2023**, *62*, e202217764.
[78] Zang, D. J.; Wang, H. Q. Polyoxometalate-based nanostructures for electrocatalytic and photocatalytic CO_2 reduction. *Polyoxometalates* **2022**, *1*, 9140006.
[79] Yin, Y. A.; Chen, W. J.; Liu, C. Y.; Zhang, M. M.; Lin, C. G.; Miras, H. N.; Song, Y. F. Supramolecular assembly of covalently modified Anderson-type polyoxometalates and crown ethers towards *pseudo*-rotaxane structures. *Polyoxometalates* **2025**, *4*, 9140081.
[80] Zhao, Q.; Mao, D. A.; Huang, L. L.; Zhou, K.; Tian, H. R.; Chen, B. K.; Bi, Y. F. Thiacalix[4]arene-functionalized molecular clusters involving the Keggin-type PM_4Mo_8 (M = Co, Ni) motif: Electrochemical and photothermal conversion properties. *Polyoxometalates* **2025**, *4*, 9140091.
[81] Wang, T.; Chen, W. C.; Liu, Q. D.; Wang, W.; Wang, Y. M.; Wu, B.; Shi, W. X.; Zhu, Y. Q.; He, P. L.; Wang, X. Self-assembly of polyoxometalate-based sub-1 nm polyhedral building blocks into rhombic dodecahedral superstructures. *Angew. Chem.* **2023**, *135*, e202314045.
[82] Zhang, F. H.; Li, H. Y.; Li, Z.; Liu, Q. D.; Wang, X. Phase engineering of polyoxometalate assembled superstructures. *Nat. Synth.* **2024**, *3*, 1039–1048.
[83] Zhang, F. H.; Li, Z.; Wang, X. Mechanically tunable organogels from highly charged polyoxometalate clusters loaded with fluorescent dyes. *Nat. Commun.* **2023**, *14*, 8327.
[84] Hu, S.; Liu, H. L.; Wang, P. P.; Wang, X. Inorganic nanostructures with sizes down to 1 nm: A macromolecule analogue. *J. Am. Chem. Soc.* **2013**, *135*, 11115–11124.
[85] Liu, H. L.; Gong, Q. H.; Yue, Y. H.; Guo, L.; Wang, X. Sub-1 nm nanowire based superlattice showing high strength and low modulus. *J. Am. Chem. Soc.* **2017**, *139*, 8579–8585.
[86] Liu, H. L.; Li, H. Y.; He, P. L.; Wang, X. Sub-1 nm nickel molybdate nanowires as building blocks of flexible paper and electrochemical catalyst for water oxidation. *Small* **2016**, *12*, 1006–1012.
[87] Zhang, S. M.; Shi, Y. A.; He, T.; Ni, B.; Li, C. Z.; Wang, X. Ultrathin tungsten bronze nanowires with efficient photo-to-thermal conversion behavior. *Chem. Mater.* **2018**, *30*, 8727–8731.
[88] Chen, Z. X.; Zhang, Y. T.; Zhao, C.; Xia, Y. X.; Li, Z. Q.; Zhou, X. P.; Xiao, L. Y.; Liu, X. F.; Zhang, Y. Tailoring graphite into subnanometer graphene. *Adv. Mater.* **2024**, *36*, 2310022.
[89] Duan, R.; Qi, W. H.; Tang, K. W.; Liu, W. M. Sub-nano cluster decoration for the manipulation of the photogenerated carrier behavior of MoS_2. *InfoMat* **2025**, *7*, e12610.
[90] Lu, H. Q.; Shen, W. F.; Wang, H. L.; Liu, J. B.; Yu, Y.; Ma, G. T.; Liu, H. G.; Wu, S.; Hu, C. G. Direct observation of crystalline distortions in mechanically exfoliated low-symmetric 2D materials. *Chem. Res. Chin. Univ.* **2023**, *39*, 666–672.

[91] Zhang, H. M.; Zhang, L. Q.; Peng, Z. D.; Zhou, J. K.; Li, L.; Wang, W. Q.; Luo, W.; Deng, C. Y.; Wang, G.; Peng, G. Synthesis of $Fe_{1+y}Te$ nanocrystals with modulated dimensionality and properties. *Adv. Funct. Mater.*, in press, DOI: 10.1002/adfm.202519365.

[92] Liu, J. L.; Shi, W. X.; Ni, B.; Yang, Y.; Li, S. Z.; Zhuang, J.; Wang, X. Incorporation of clusters within inorganic materials through their addition during nucleation steps. *Nat. Chem.* **2019**, *11*, 839–845.

[93] Whitehead, C. B.; Özkar, S.; Finke, R. G. LaMer's 1950 Model for particle formation of instantaneous nucleation and diffusion-controlled growth: A historical look at the model's origins, assumptions, equations, and underlying sulfur sol formation kinetics data. *Chem. Mater.* **2019**, *31*, 7116–7132.

[94] Xia, Y. N.; Xiong, Y. J.; Lim, B.; Skrabalak, S. E. Shape-controlled synthesis of metal nanocrystals: Simple chemistry meets complex physics? *Angew. Chem., Int. Ed.* **2008**, *48*, 60–103.

[95] Liu, J. L.; Shi, W. X.; Wang, X. Cluster-nuclei coassembled into two-dimensional hybrid CuO-PMA sub-1 nm nanosheets. *J. Am. Chem. Soc.* **2019**, *141*, 18754–18758.

[96] Liu, J. L.; Shi, W. X.; Nie, S. Y.; Wang, X. Functionally guided precise synthesis of manganous oxide-polyoxometalate 2D hybrid sub-1 nm nanosheet superstructures. *Small Struct.* **2022**, *3*, 2200039.

[97] Liu, J. L.; Shi, W. X.; Wang, X. ZnO-POM cluster sub-1 nm nanosheets as robust catalysts for the oxidation of thioethers at room temperature. *J. Am. Chem. Soc.* **2021**, *143*, 16217–16225.

[98] Yuan, G. B.; Ge, H. Y.; Shi, W. X.; Liu, J. L.; Zhang, Y.; Wang, X. Hybrid sub-1 nm nanosheets of Co-assembled $MnZnCuO_x$ and polyoxometalate clusters as anodes for Li-ion batteries. *Angew. Chem., Int. Ed.* **2023**, *62*, e202309934.

[99] Liu, J. L.; Liu, N.; Wang, H. W.; Shi, W. X.; Zhuang, J.; Wang, X. Hybrid MoO_3-polyoxometallate sub-1 nm nanobelt superstructures. *J. Am. Chem. Soc.* **2020**, *142*, 17557–17563.

[100] Zhang, S. M.; Liu, N.; Wang, H. W.; Lu, Q. C.; Shi, W. X.; Wang, X. Sub-nanometer nanobelts based on titanium dioxide/zirconium dioxide-polyoxometalate heterostructures. *Adv. Mater.* **2021**, *33*, 2100576.

[101] Zhang, S. M.; Lu, Q. C.; Yu, B.; Cheng, X. J.; Zhuang, J.; Wang, X. Polyoxometalates facilitating synthesis of subnanometer nanowires. *Adv. Funct. Mater.* **2021**, *31*, 2100703.

[102] Ge, H. Y.; Shi, W. X.; Liu, J. L.; Zhang, Y.; Wang, X. High entropy oxide-polyoxometalate sub-1 nm hetero-nanowires as cathode catalysts in Li–O_2 batteries. *J. Am. Chem. Soc.* **2025**, *147*, 8367–8376.

[103] Yuan, G. B.; Shi, W. X.; Shang, Z. A.; Chen, W. X.; Sun, Z. Y.; Liu, J. L.; Zhang, Y.; Wang, X. Polyoxometalate induced bismuth sulfide sub-1 nm nanowires as efficient photocathodes in Li-CO_2 batteries. *Small*, in press, DOI:10.1002/smll.202514807.

[104] Liu, Z.; Goudeli, E.; Guo, R.; Xie, H. T.; Luo, Q. J.; Zhao, L. C.; Xu, W. J.; Richardson, J. J.; Xu, W. J.; Caruso, F. et al. Flame synthesis achieves compositionally tailorable high-entropy metal-containing nanomaterials. *Nat. Chem.* **2025**, *17*, 1497–1504.

[105] Shahbazi, H.; Seraji, P.; Farraj, H.; Yang, T. M.; Kim, A.; Fattahpour, S.; Papailias, I.; Diamond, M.; Namvar, S.; Ahmadiparidari, A. et al. Resiliency, morphology, and entropic transformations in high-entropy oxide nanoribbons. *Science* **2025**, *388*, 950–956.

[106] Song, M.; Zhang, X. L.; Wan, S.; Wang, G.; Liu, J. X.; Li, W. W.; Dong, H. L.; Lou, C. J.; Chen, Z. Q.; Chen, B. et al. Electrical conductivities and conduction mechanism of lithium-doped high-entropy oxides at different temperature and pressure conditions. *JACS Au* **2024**, *4*, 592–606.

[107] Ge, H. Y.; Zheng, L. R.; Yuan, G. B.; Shi, W. X.; Liu, J. L.; Zhang, Y.; Wang, X. Polyoxometallate cluster induced high-entropy oxide sub-1 nm nanosheets as photoelectrocatalysts for Zn-air batteries. *J. Am. Chem. Soc.* **2024**, *146*, 10735–10744.

[108] Liu, Q. D.; He, S. Q.; Yu, B.; Cheng, X. J.; Shi, W. X.; Wang, X. Visible light induced Ag-polyoxometalate coassembly into single-cluster nanowires. *Adv. Mater.* **2022**, *34*, 2206178.

[109] Liu, Q. D.; He, P. L.; Yu, H. D.; Gu, L.; Ni, B.; Wang, D.; Wang, X. Single molecule-mediated assembly of polyoxometalate single-cluster rings and their three-dimensional superstructures. *Sci. Adv.* **2019**, *5*, eaax1081.

[110] Liu, Q. D.; Zhang, Q. H.; Shi, W. X.; Hu, H. S.; Zhuang, J.; Wang, X. Self-assembly of polyoxometalate clusters into two-dimensional clusterphene structures featuring hexagonal pores. *Nat. Chem.* **2022**, *14*, 433–440.

[111] Ewan, T. The industrial applications of electro-chemistry. *Nature* **1898**, *58*, 112–115.

[112] Thomson, W. A constant form of daniell's battery. *Nature* **1871**, *3*, 350–351.

[113] Saunder, S. A. On the variations of the electromotive force of a new form of leclanché's cell. *Nature* **1875**, *12*, 564–565.

[114] Lopes, P. P.; Stamenkovic, V. R. Past, present, and future of lead-acid batteries. *Science* **2020**, *369*, 923–924.

[115] Yang, M. Z.; Li, H. Y.; Wang, J.; Shi, W. X.; Zhang, Q. H.; Xing, H. Z.; Ren, W. B.; Sun, B. Z.; Guo, M. F.; Xu, E. X. et al. Roll-to-roll fabricated polymer composites filled with subnanosheets exhibiting high energy density and cyclic stability at 200 °C. *Nat. Energy* **2024**, *9*, 143–153.

[116] Shang, Q. Q.; Shen, K. Q.; Zhao, D. Y.; Wang, X. Y.; Wei, Y. T.; Wang, H. Y.; Wang, G.; Zhang, D. D.; Niu, J. Y. Rare-earth-induced peroxo-phosphotungstates: Enhanced proton conductivity in corresponding membranes. *Polyoxometalates* **2025**, *4*, 9140077.

[117] Cao, X. W.; Ma, C.; Luo, L.; Chen, L.; Cheng, H.; Orenstein, R. S.; Zhang, X. W. Nanofiber materials for lithium-ion batteries. *Adv. Fiber Mater.* **2023**, *5*, 1141–1197.

[118] Cheng, M. Z.; Chen, A. Y.; Zhang, Z. J.; Sheng, C. C.; Zhou, H. S.; He, P. Regulating lithium intercalation/plating competition To enhance low-temperature performance of Li-ion batteries. *J. Am. Chem. Soc.* **2025**, *147*, 40776–40787.

[119] Pandya, R.; Valzania, L.; Dorchies, F.; Xia, F.; Mc Hugh, J.; Mathieson, A.; Tan, H. J.; Parton, T. G.; Godeffroy, L.; Mazloomian, K. et al. Three-dimensional operando optical imaging of particle and electrolyte heterogeneities inside Li-ion batteries. *Nat. Nanotechnol.* **2023**, *18*, 1185–1194.

[120] Yang, Q.; Cai, J. Y.; Li, G. W.; Gao, R. H.; Han, Z. Y.; Han, J. J.; Liu, D.; Song, L. X.; Shi, Z. X.; Wang, D. et al. Chlorine bridge bond-enabled binuclear copper complex for electrocatalyzing lithium-sulfur reactions. *Nat. Commun.* **2024**, *15*, 3231.

[121] Zhong, W.; He, R. J.; Peng, L. F.; Liu, W.; Peng, J. Y.; Zhu, H. L.; Xiang, J. Y.; Cheng, S. J.; Xie, J. Lifecycle synergistic prelithiation strategy of both anode and cathode for high-performance lithium-ion batteries. *Adv. Energy Mater.* **2025**, *15*, 2406007.

[122] Ai, B.; Zhao, W. R.; Li, M. L.; Zhang, W.; Mei, D. H.; Yu, J. H. Surface-conducting lithium superionic conductors for solid-state batteries. *J. Am. Chem. Soc.* **2025**, *147*, 11072–11079.

[123] Banerjee, S.; Tkatchenko, A. Non-local interactions determine local structure and lithium diffusion in solid electrolytes. *Nat. Commun.* **2025**, *16*, 1672.

[124] Lei, Z. H.; Chen, L. K.; Lou, C. J.; Zhang, F. Q.; Liu, W. J.; Peng, K.; Li, X. D.; Li, Y. H.; He, Y. B.; Kang, F. Y. et al. Coupling coordination structures and superionic lithium conduction in amorphous oxyhalide solid-state electrolytes. *J. Am. Chem. Soc.* **2025**, *147*, 43992–44001.

[125] Song, Y.; Qu, H. T.; Lao, Z. J.; Xiao, X.; Lu, G. X.; Song, Y. Z.; Nie, L.; Wang, J.; Yang, J. L.; Zhu, Y. F. et al. Creating vacancy strong interaction to enable homogeneous high-throughput ion transport for efficient solid-state lithium batteries. *Adv. Mater.* **2025**, *37*, 2419271.

[126] Ma, J.; Xiang, Y.; Xu, J. Y.; Zhang, W. F.; Zhang, H. M.; Qiu, J. Y.; Zhu, X. Y.; Zhang, H.; Lin, H. P.; Cao, G. P. Reducing lithium-diffusion barrier on the wadsley-roth crystallographic shear plane via low-valent cation doping for ultrahigh power lithium-ion batteries. *Adv. Energy Mater.* **2025**, *15*, 2403623.

[127] Rahman, M. M.; Bisht, A.; Amin, R.; Abouimrane, A.; Kweon, C. B. M.; Belharouak, I. Thermal dynamics and lithium plating detection in high-power Li-ion batteries for eVTOL applications. *Adv. Energy Mater.* **2025**, *15*, e03292.

[128] Zhang, X.; Ju, Z. Y.; Zhu, Y.; Takeuchi, K. J.; Takeuchi, E. S.; Marschilok, A. C.; Yu, G. H. Multiscale understanding and architecture design of high energy/power lithium-ion battery electrodes. *Adv. Energy Mater.* **2021**, *11*, 2000808.

[129] Huang, X. Y.; Zhao, C. Z.; Kong, W. J.; Yao, N.; Shuang, Z. Y.; Xu, P.; Sun, S.; Lu, Y.; Huang, W. Z.; Li, J. L. et al. Tailoring polymer electrolyte solvation for 600 Wh kg^{-1} lithium batteries. *Nature* **2025**, *646*, 343–350.

[130] Li, J. X.; Liang, G. M.; Zheng, W.; Zou, J. S.; Wang, C. Y.; Yuwono, J. A.; Fan, Y. M.; Johannessen, B.; Thomsen, L.; Hu, S. J. et al. Structure flexibility enabled by surface high-concentration titanium doping for durable lithium-ion battery cathodes. *J. Am. Chem. Soc.* **2025**, *147*, 18606–18617.

[131] Zhao, C. X.; Wang, Z. i.; Jacobson, D.; Li, Y.; Khaykovich, B.; Fayfar, S.; Zheng, L.; LaManna, J.; Chen, X. L.; Hussey, D. S. et al. Electrolytes that reduce electro-osmotic drag improve fast charging of lithium-ion batteries. *Science* **2025**, *390*, 745–750.

[132] Wei, Y. N.; Wang, M.; Zhang, M. M.; Cai, T.; Huang, Y. H.; Xu, M. Advancements, challenges, and future trajectories in advanced battery safety detection. *Electrochem. Energy Rev.* **2025**, *8*, 10.

[133] Chen, Z. D.; Luo, Y. T.; Yang, D. S.; Hu, Y. H.; Hou, H. R.; Koratkar, N.; Zhou, G. M.; Liu, W. Intraparticle alloying-plating reaction for high-performing lithium metal batteries with low volume expansion. *Mater. Today* **2025**, *86*, 74–86.

[134] Chiang, C. H.; Chen, H. T.; Chen, W. Y.; Wang, W. T.; Feng, S. P.; Wu, C. G. Tin oxide/amphiphilic polymer double-layered hole transporter for high-efficiency tin perovskite solar modules. *Adv. Energy Mater.* **2024**, *14*, 2400346.

[135] Qiao, D. D.; Wei, X. Z.; Zhu, J. G.; Zhang, G. X.; Yang, S.; Wang, X. Y.; Jiang, B.; Lai, X.; Zheng, Y. J.; Dai, H. F. Mechanism of battery expansion failure due to excess solid electrolyte interphase growth in lithium-ion batteries. *eTransportation* **2025**, *25*, 100450.

[136] Bai, P. D.; Li, H. Q.; Zhao, W. L.; Hu, H. B.; Wang, M. Y.; Hu, H.; Liang, Z. X.; Dong, H. Y.; Sun, J. Y.; Lian, L. F. et al. Orientation-engineered anderson-type polyoxometalate sub-1 nm nanosheets for high-performance lithium-ion battery anodes. *Angew. Chem., Int. Ed.*, in press, DOI: 10.1002/anie.202520296.

[137] Cheng, Y.; Liu, X. W.; Xiao, X. D.; Du, L. L.; Zhang, H.; Yang, Y. K.; Xu, L. Yb_2O_3-polyoxometalate sub-1 nm heterogeneous cluster chains with local electron rearrangement for accelerated Li^+ transport in composite solid electrolytes. *Small* **2025**, *21*, 2501010.

[138] Liu, Y. C.; Zhou, X. G.; Qiu, T. Y.; Yao, R. Q.; Yu, F. Y.; Song, T. T.; Lang, X. Y.; Jiang, Q.; Tan, H. Q.; Li, Y. Q. et al. Co-assembly of polyoxometalates and porphyrins as anode for high-performance lithium-ion batteries. *Adv. Mater.* **2024**, *36*, 2407705.

[139] Meng, Y. F.; Han, R.; Wang, Y.; Tian, Y.; Ma, M. Y.; Zhao, Y.; Li, B. H.; Fan, X. L.; Kang, F. Y.; Aurbach, D. et al. Chlorinated-solvent-based electrolyte for safe and stable lithium battery chemistry. *Angew. Chem., Int. Ed.* **2026**, *65*, e16987.

[140] Yang, C.; Zhou, X.; Sun, R. T.; Hu, W. X.; Wang, M. L.; Dong, X. L.; Piao, N.; Han, J.; Chen, W.; You, Y. A safe electrolyte enriched with flame-retardant solvents for high-voltage $LiCoO_2$||graphite pouch cells. *ACS Energy Lett.* **2024**, *9*, 5364–5372.

[141] Zhang, W. F.; Feng, X. N.; Huang, W. S.; Lu, L. G.; Wang, H. W.; Wang, L.; He, X. M.; Wei, M. D.; Ouyang, M. G. Thermal runaway inhibition of lithium-ion batteries employing thermal-driven phosphazene based electrolytes. *Adv. Funct. Mater.* **2025**, *35*, 2508688.

[142] Liu, C.; Reed, S.; Manthiram, A. Delineating the triphasic side reaction products in high-energy density lithium-ion batteries. *Adv. Mater.* **2025**, *37*, e09889.

[143] Liu, Y. K.; Zhao, C. Z.; Du, J.; Zhang, X. Q.; Chen, A. B.; Zhang, Q. Research progresses of liquid electrolytes in lithium-ion batteries. *Small* **2023**, *19*, 2205315.

[144] Wang, C. Y.; Qin, K. Q.; Ge, S. H.; Gupta, N.; Sasaki, T.; Aotani, K. Metrics for evaluating safe electrolytes in energy-dense lithium batteries. *Nat. Energy* **2025**, *10*, 1382–1390.

[145] Dutra, A. C. C.; Goldmann, B. A.; Islam, M. S.; Dawson, J. A. Understanding solid-state battery electrolytes using atomistic modelling and machine learning. *Nat. Rev. Mater.* **2025**, *10*, 566–583.

[146] Zhao, F. P.; Zhang, S. M.; Wang, S.; Reid, J. W.; Xia, W.; Liu, J.; King, G.; Kaduk, J. A.; Liang, J. W.; Luo, J. et al. Anion sublattice design enables superionic conductivity in crystalline oxyhalides. *Science* **2025**, *390*, 199–204.

[147] Zou, Z. W.; Xiao, Z. X.; Lin, Z. K.; Zhang, B. C.; Zhang, C. X.; Wei, F. Lithium phosphorous oxynitride as an advanced solid-state electrolyte to boost high-energy lithium metal battery. *Adv. Funct. Mater.* **2024**, *34*, 2409330.

[148] Chen, Y.; Qian, J.; Wang, K.; Li, L.; Wu, F.; Chen, R. J. Cutting-edge developments at the interface of inorganic solid-state electrolytes. *Adv. Mater.* **2025**, *37*, 2502653.

[149] Liu, Z. T.; Chien, P. H.; Wang, S.; Song, S. W.; Lu, M.; Chen, S.; Xia, S. M.; Liu, J.; Mo, Y. F.; Chen, H. L. Tuning collective anion motion enables superionic conductivity in solid-state halide electrolytes. *Nat. Chem.* **2024**, *16*, 1584–1591.

[150] Wang, C. Y.; He, Y. B.; Zou, P. C.; He, Q.; Li, J.; Xin, H. L. Nanoscale origin of the soft-to-hard short-circuit transition in inorganic solid-state electrolytes. *J. Am. Chem. Soc.* **2025**, *147*, 19084–19092.

[151] Balaish, M.; Gonzalez-Rosillo, J. C.; Kim, K. J.; Zhu, Y. T.; Hood, Z. D.; Rupp, J. L. M. Processing thin but robust electrolytes for solid-state batteries. *Nat. Energy* **2021**, *6*, 227–239.

[152] Xiao, Z. X.; Zou, Z. W.; Zhao, K. H.; Lin, Z. K.; Zhang, B. C.; Yu, Y. X.; Zhu, C.; Xu, K.; Xing, L. D.; Li, W. S. Inhibiting interfacial failure in garnet-based solid-state batteries with high-capacity anodes: Mechanism and strategies. *Adv. Mater.* **2025**, *37*, 2507188.

[153] Chen, H.; Chen, K. A.; Yang, J. Y.; Liu, B. L.; Luo, L. B.; Li, H.; Chen, L.; Zhao, A. L.; Liang, X. M.; Feng, J. W. et al. Designing advanced electrolytes for high-safety and long-lifetime sodium-ion batteries via anion-cation interaction modulation. *J. Am. Chem. Soc.* **2024**, *146*, 15751–15760.

[154] Ruan, J. F.; Hu, J. M.; Li, Q.; Luo, S. N.; Yang, J. Y.; Liu, Y.; Song, Y.; Zheng, S. Y.; Sun, D. L.; Fang, F. et al. Current collector interphase design for high-energy and stable anode-less sodium batteries. *Nat. Sustain.* **2025**, *8*, 530–541.

[155] Wang, Y. H.; Yan, J. X.; Xie, B. X.; Meng, Y.; Fu, C. K.; Kong, F. P.; Wang, X. Y.; Zhou, Q. J.; Chen, X.; Li, J. T. et al. Tuning cyanide coordination electronic structure enables stable Prussian blue analogues for sodium-ion batteries. *Nat. Commun.* **2025**, *16*, 10083.

[156] Chen, Z. Y.; Yang, L. H.; Yu, G.; Yang, R.; Zhao, Y.; Liu, C. G.; Zhang, F.; Tang, Y. B. Progress and prospects in sodium-ion battery anode materials: From fundamentals to material engineering strategies. *Energy Storage Mater.* **2026**, *84*, 104745.

[157] Deng, W. J.; Yang, H.; Huo, H. Y.; Yu, Y. Recent advances, key strategies, and challenges in fast-charging hard carbon anodes for sodium-ion batteries. *Adv. Funct. Mater.* **2025**, *35*, 2504168.

[158] Wu, Y. R.; Xu, R. N.; Xiao, Z.; Wang, Z. Y.; Zheng, R. G.; Song, Z. S.; Liu, Y. G. The hidden aspects of batteries: Mechanisms, strategies, challenges and future directions of gas generation in sodium-ion batteries. *Adv. Funct. Mater.* **2025**, *35*, 2423478.

[159] Huang, Y. F.; Li, T. Z.; Wu, Z. Z.; Yang, W.; Liu, Z. D.; Gan, J. Y.; Zou, R.; Iwuoha, E.; Feleni, U.; Ren, J. W. et al. Ultrahigh-efficiency zinc-air batteries enabled by defect-engineered biomass carbon and dynamic nickel redox mediation. *Adv. Mater.*, in press, DOI: 10.1002/adma.202513768.

[160] Li, J. X.; Zhang, K.; Wang, B. J.; Peng, H. S. Light-assisted metal-air batteries: Progress, challenges, and perspectives. *Angew. Chem., Int.*

Ed. **2022**, *61*, e202213026.
[161] Park, H.; Kang, M.; Lee, D.; Park, J.; Kang, S. J.; Kang, B. Activating reversible carbonate reactions in Nasicon solid electrolyte-based Na-air battery via *in-situ* formed catholyte. *Nat. Commun.* **2024**, *15*, 2952.
[162] Wang, Q. C.; Chu, B. X.; Shang, C. Y.; Shao, B.; Yang, F.; Dang, D.; Li, L.; Gu, M.; Xiao, X.; Xu, Q. Asymmetric Mn/Fe dual single-atom catalysts for pH-universal oxygen electroreduction and sustainable metal-air batteries. *Adv. Mater.* **2025**, *37*, e14343.
[163] Liang, S.; Song, L. N.; Wang, X. X.; Wang, Y.; Wang, H. F.; Feng, L.; Xu, J. J. Efficient carrier separation via Ru@TS@C zeolite: Enabling photo-cathodes for high-efficiency photo-assisted metal-air batteries. *Angew. Chem., Int. Ed.* **2025**, *64*, e202512477.
[164] Luo, M. H.; Sun, W. P.; Xu, B. B.; Pan, H. G.; Jiang, Y. Z. Interface engineering of air electrocatalysts for rechargeable zinc-air batteries. *Adv. Energy Mater.* **2021**, *11*, 2002762.
[165] Zheng, L. J.; Song, L. N.; Wang, X. X.; Liang, S.; Wang, H. F.; Du, X. Y.; Xu, J. J. Intrinsic stress-strain in barium titanate piezocatalysts enabling lithium-oxygen batteries with low overpotential and long life. *Angew. Chem., Int. Ed.* **2023**, *62*, e202311739.
[166] Liu, T.; Zhao, S. Y.; Xiong, Q.; Yu, J.; Wang, J.; Huang, G.; Ni, M.; Zhang, X. B. Reversible discharge products in Li-air batteries. *Adv. Mater.* **2023**, *35*, 2208925.
[167] Yin, W. W.; Zhi, X.; Li, Y. Y.; Ma, J. W.; Johannessen, B.; Xie, F. X.; Wu, M. M. Bimetallic alloy air cathode promoting superoxide formation for high-performance Na-air batteries. *Small* **2025**, *21*, 2500109.
[168] Zhang, Y.; Zhang, S. T.; Li, H. N.; Lin, Y. R.; Yuan, M. W.; Nan, C. Y.; Chen, C. Tunable oxygen vacancies of cobalt oxides in lithium-oxygen batteries: Morphology control of discharge product. *Nano Lett.* **2023**, *23*, 9119–9125.
[169] He, T.; Chen, Y.; Liu, Q. M.; Lu, B. Z.; Song, X. W.; Liu, H. T.; Liu, M.; Liu, Y. N.; Zhang, Y.; Ouyang, X. P. et al. Theory-guided regulation of FeN_4 spin state by neighboring Cu atoms for enhanced oxygen reduction electrocatalysis in flexible metal-air batteries. *Angew. Chem., Int. Ed.* **2022**, *61*, e202201007.
[170] Song, L. N.; Zheng, L. J.; Wang, X. X.; Kong, D. C.; Wang, Y. F.; Wang, Y.; Wu, J. Y.; Sun, Y.; Xu, J. J. Aprotic lithium-oxygen batteries based on nonsolid discharge products. *J. Am. Chem. Soc.* **2024**, *146*, 1305–1317.
[171] Liu, J.; Li, Y. J.; Ding, Y. J.; Wu, L. S.; Qin, J. Q.; Chen, T. L.; Meng, C. X.; Zhou, F.; Ma, X. K.; Wu, Z. S. A bifunctional imidazolyl iodide mediator of electrolyte boosts cathode kinetics and anode stability towards low overpotential and long-life Li–O_2 batteries. *Angew. Chem., Int. Ed.* **2025**, *64*, e202421107.
[172] Wu, J.; Shi, J. W.; Li, Z. Z.; Li, M. H.; Pan, K. C.; Dou, Y. Y.; Tian, Y.; Zhang, Z.; Zhou, Z. Framework integration for adaptive interfaces in flexible solid-state lithium-oxygen batteries. *Angew. Chem., Int. Ed.* **2025**, *64*, e202507660.
[173] Karunarathne, S.; Sandaruwan, C.; Kannangara, Y. Y.; Demko, D.; Orange, F.; Mija, A.; Kamai, A. R.; Abdelkader, A. M. Triphase heterogeneous electrocatalysts of Ni and Co for high-performing Li–O_2 batteries. *EcoMat* **2025**, *7*, e70002.
[174] Kim, B.; Shin, K.; Henkelman, G.; Ryu, W. H. CO_2-mediated porphyrin catalysis in reversible Li–CO_2 cells. *Chem. Eng. J.* **2023**, *477*, 147141.
[175] Li, L.; Hua, M. H.; Li, J. F.; Zhang, P.; Nie, Y. J.; Wang, P.; Lin, X. H.; Zhang, Z. W.; Wang, R. T.; Ge, X. L. et al. Tuning dual catalytic active sites of Pt single atoms paired with high-entropy alloy nanoparticles for advanced Li–O_2 batteries. *ACS Nano* **2025**, *19*, 4391–4402.
[176] Zhang, N. B.; Yin, L. M.; Chen, L. T.; Ma, B. B.; Li, Y. T. H.; Zhang, X. Y.; Liu, J. Q.; Zhou, Z. Size- and crystallinity-dependent oxygen vacancy engineering to modulate Fe active sites for enhanced reversible nitrogen fixation in Lithium-nitrogen batteries. *Energy Storage Mater.* **2025**, *76*, 104171.
[177] Zhao, N.; Liu, L. M.; Lu, X.; Li, Y. Y.; Wu, X. S.; Peng, S. C.; Wei, J. W.; Gao, Y.; Zhang, H. Q.; Fan, Y. M. et al. Elevating discharge voltage of Li_2CO_3-routine Li–CO_2 battery over 2.9 V at an ultra-wide temperature window. *Angew. Chem., Int. Ed.* **2024**, *63*, e202407303.
[178] Guan, H. M.; Cai, Z. P.; Wu, X. Y.; Wang, K. X.; Chen, J. S. Unlocking the power of lewis basicity in oxide lattice oxygens: A regulating force for enhanced oxygen evolution kinetics in Li–O_2 batteries. *Angew. Chem., Int. Ed.* **2025**, *64*, e202509132.
[179] Zeng, Y. C.; Zhou, Y.; Liu, F. Z.; Li, H. B. Unlocking the orbital interaction mode in Li–O_2 batteries. *Angew. Chem., Int. Ed.*, in press, DOI: 10.1002/anie.202520062.
[180] Zhou, Y.; Yin, K.; Huang, Y. Y.; Li, J. P.; Zhu, A. Q.; Lin, D. W.; Gan, G. Q.; Zhang, J. F.; Liu, K.; Zhang, T. et al. D-orbital reconstruction achieves low charge overpotential in Li-oxygen batteries. *Nat. Commun.* **2025**, *16*, 3353.
[181] Noked, M.; Schroeder, M. A.; Pearse, A. J.; Rubloff, G. W.; Lee, S. B. Protocols for evaluating and reporting Li–O_2 cell performance. *J. Phys. Chem. Lett.* **2016**, *7*, 211–215.
[182] Chang, Y. H.; Tseng, I. H.; Pourzolfaghar, H.; Lin, S. H.; Li, Y. Y. Atomic engineering of bifunctional core-shell catalysts with dual single-atom and cobalt nanoparticles for boosting ORR and OER kinetics in Zn-air batteries. *Small* **2025**, *21*, e06084.
[183] Yang, X.; Zhu, B. H.; Gao, Z. Y.; Yang, C.; Zhou, J. B.; Han, A. J.; Liu, J. F. A vacuum vapor deposition strategy to Fe single-atom catalysts with densely active sites for high-performance Zn-air battery. *Adv. Sci.* **2024**, *11*, 2306594.
[184] You, H. H.; Xu, Y. F.; Shao, T.; Wu, D. S.; Sun, F. F.; Cao, R.; Cao, M. N. Enhanced bifunctional catalysis of iridium nanoparticles on nitrogen-doped holey carbon via strong metal-support interaction for rechargeable zinc-air batteries. *Angew. Chem., Int. Ed.* **2025**, *64*, e202514873.
[185] Liu, H. Q.; Huang, J. Z.; Feng, K.; Xiong, R.; Ma, S. Y.; Wang, R.; Fu, Q.; Rafique, M.; Liu, Z. G.; Han, J. C. et al. Reconstructing the coordination environment of Fe/Co dual-atom sites towards efficient oxygen electrocatalysis for Zn-air batteries. *Angew. Chem., Int. Ed.* **2025**, *64*, e202419595.
[186] Wang, R. Y.; Gao, M. Z.; Zhao, G. C.; Chen, J. C.; Guo, Z. Y.; Wang, Y. G. Photo- and electrocatalytic dual-layer cathode facilitating Zn peroxide chemistry in near-neutral Zn-air batteries. *J. Am. Chem. Soc.* **2025**, *147*, 8205–8214.
[187] Zhi, T. J.; Li, Y.; Yi, Z. X.; Zhu, S. G.; Zhang, L. Pyrolysis-mediated polycyano strategy for directed construction of Fe_3C-synergized Fe–N carbon nanotubes heterostructure toward high-efficiency oxygen reduction reaction. *Small* **2025**, *21*, e08558.
[188] Liu, P. X.; Wang, Y. Q.; Lv, R. J.; Zhang, G. Y.; Liu, X.; Wang, L. Design principles of non-noble metal catalysts for high-performance rechargeable Zn-air batteries. *Energy Storage Mater.* **2025**, *76*, 104155.
[189] Chen, S.; Shang, J. T.; Peng, F. E.; Song, Z. H.; Zheng, Y.; Dai, Y. H.; Zhu, J. X.; Guo, F.; Fu, X. L.; Chu, K. B. et al. Covalent-bridged heterointerfaces via grafted triazine organic polymers enable directed charge transfer for efficient oxygen reduction in Zn-air batteries. *ACS Nano* **2025**, *19*, 31870–31881.
[190] Guo, M.; Wang, L. X.; Huang, Z. Y.; Li, H. T.; Isimjan, T. T.; Yang, X. L. Modulating the energy barrier via the synergism of Cu_3P and CoP to accelerate kinetics for bolstering oxygen electrocatalysis in Zn-air batteries. *ACS Nano* **2024**, *18*, 17901–17912.
[191] Hao, G. W.; Wang, P.; Deng, D. J.; Zhang, W.; Wu, S. Q.; Zhang, W. H.; Li, H. N.; Xu, L. Surface microenvironment regulation of nitrogen-doped carbon via deep eutectic solvent for enhanced oxygen reaction kinetics in zinc-air batteries. *Chem. Eng. Sci.* **2026**, *321*, 122738.
[192] Lu, H. F.; Zhang, D.; Jin, Q. Z.; Zhang, Z. L.; Lyu, N. W.; Zhu, Z. J.; Duan, C. X.; Qin, Y.; Jin, Y. Gradient electrolyte strategy achieving long-life zinc anodes. *Adv. Mater.* **2023**, *35*, 2300620.
[193] Yan, C.; Zhu, L.; Li, P.; Tang, J.; He, H. B.; Zhu, Y. Q.; Li, D. D.

Multi-level Zn^{2+}-buffering interphase enabled by hierarchical nanostructure engineering of gel polymers for highly reversible zinc metal anode. *Adv. Mater*., in press, DOI: 10.1002/adma.202515316.

[194] Zhang, X. M.; Tang, Q.; Luo, H.; Xu, Y. L.; Miao, S. C.; Zhou, S. Y.; Xu, C. H. Y.; Jia, Y.; He, Q. J.; Peng, J. N. et al. Hydrogen bond reconstruction maneuver in eutectic electrolyte enables ultralong-lifespan zinc-ion batteries. *J. Am. Chem. Soc.* **2025**, *147*, 39440–39451.

[195] Ruan, P. C.; Liang, S. Q.; Lu, B. G.; Fan, H. J.; Zhou, J. Design strategies for high-energy-density aqueous zinc batteries. *Angew. Chem., Int. Ed.* **2022**, *61*, e202200598.

[196] Xiao, Z. Q.; Liu, Z. X.; Wu, X. R.; Xiao, X.; Liu, Y. N.; Liu, J. C.; Zheng, Z. Y.; Yao, W. X.; Li, J. C.; Zhou, G. M. Artificial protrusion architectures enabling horizontal-diffusion nucleation for stable zinc-based batteries. *J. Am. Chem. Soc.* **2025**, *147*, 32216–32224.

[197] Zhou, L. J.; Li, P.; Zeng, C. H.; Yi, A.; Xie, J. H.; Wang, F. X.; Zheng, D. Z.; Liu, Q.; Lu, X. H. Unraveling the mechanism of cooperative redox chemistry in high-efficient Zn^{2+} storage of vanadium oxide cathode. *Adv. Sci.* **2024**, *11*, 2305749.

[198] Ge, H. Y.; Zhang, F. H.; Hao, Z. M.; Liu, J. L.; Zhang, Y.; Wang, X. A universal strategy to increase the mechanical performance of polymer-inorganic composites by sub-1 nm hetero-nanowires. *Adv. Funct. Mater.* **2025**, *35*, 2422768.

[199] Luo, R. H.; Zheng, X. H.; Jiang, T. L.; Shen, D. Y.; Wang, M. M.; Ali, M.; Liu, H. X.; Zhang, Z. D.; Feng, Y. C.; Hazoor, S. et al. Reshaping electrical double layer via synergistic dual additives for Ah-level zinc battery. *Adv. Energy Mater.* **2025**, *15*, 2501658.

[200] Tang, M. C.; Liu, Q.; Zou, X. H.; Zhang, B.; An, L. High-energy-density aqueous zinc-ion batteries: Recent progress, design strategies, challenges, and perspectives. *Adv. Mater.* **2025**, *37*, 2501361.

[201] Zheng, X. Y.; Zhu, H. T.; Wang, Z. Q.; Yang, H.; Li, R. H.; Luo, W.; Kan, W. H.; Dai, Y. M.; Zhang, H. K.; Wang, J. Z. et al. Nanoengineered aqueous-hydrotrope hybrid liquid electrolyte solutions for efficient zinc batteries across a wide temperature range. *Nat. Nanotechnol*., in press, DOI: 10.1038/s41565-025-02060-6.

[202] Guo, H. L.; Kong, J. Y.; Wang, S. X.; Li, H. J.; Zhang, E. H.; Gao, F. X.; Lin, X.; Gong, M.; Zhang, L.; Wang, D. R. Polyacrylonitrile/polyimide hybrid nanofiber separator for energy-dense aqueous zinc-ion batteries. *ACS Appl. Mater. Interfaces* **2025**, *17*, 54774–54785.

[203] Li, X. X.; Li, J. Y.; Yang, Q.; Feng, J. Z.; Wang, X. Y.; Ye, L. H.; Liu, Z. Q.; Jiang, N.; Duan, Y. T.; Tao, Z., et al. Homogenizing Zn^{2+} transport and deposition by molecular aggregation state regulation of cellulose separator for high-performance aqueous Zn-ion batteries. *Adv. Funct. Mater.* **2025**, *36*, e19947.

[204] Chen, K.; Zhang, D.; Shen, X.; Feng, X. N.; Cheng, X. B.; Wu, Y. P. Emerging thermal safety characteristics of large-capacity lithium iron phosphate lithium-ion batteries. *Adv. Energy Mater.* **2026**, *16*, e03248.

[205] Meng, F. B.; Li, Y. W.; Lin, W. H.; Chen, J. H.; Zeng, Y. Z.; Xia, Y. H.; Yuan, B.; Chen, H.; Hu, R. Z. Recycling spent lithium-ion layered cathodes: Toward direct single-crystalline regeneration technology. *Adv. Energy Mater.* **2026**, *16*, e04206.

[206] Xia, M.; Chen, J. N.; Wu, W. H.; Hu, Z.; Jin, Y. T.; He, Z. N.; Pan, L. X.; Zhang, Z. R.; Yang, T. Y.; Wang, H. S. et al. Quantitative and non-destructive analysis of failure process of pouch lithium metal batteries. *Adv. Mater. Energy* **2025**, *15*, e03858.

[207] Li, M.; Huang, X. Z.; Su, C. C.; Amine, K. Concerted formation of reversibly precipitated sulfur species and its importance for lean electrolyte lithium-sulfur batteries. *J. Am. Chem. Soc.* **2024**, *146*, 23182–23193.

[208] Zhang, K. Y.; Cui, L. K.; Liu, L.; Zhao, Y.; Niu, B.; Long, D. H.; Zhang, Y. Y. Orchestrating site-specific redox catalysis via dual-atom engineering for enhanced polysulfide conversion in high-performance Li–S batteries. *ACS Nano* **2025**, *19*, 34204–34216.

[209] Kim, J. K. Hybrid gel polymer electrolyte for high-safety lithium-sulfur batteries. *Mater. Lett.* **2017**, *187*, 40–43.

[210] Shao, Y. H.; Pang, B. Y.; Bird, L.; Robinson, J. B.; Shearing, P. R. Contemporary trends in lithium-sulfur battery design: A comparative review of liquid, quasi-solid, and all-solid-state architectures and mechanisms. *Adv. Energy Mater.* **2026**, *16*, e03239.

[211] Zhang, J.; Chou, J.; Luo, X. X.; Yang, Y. M.; Yan, M. Y.; Jia, D.; Zhang, C. H.; Wang, Y. H.; Wang, W. P.; Tan, S. J. et al. A fully amorphous, dynamic cross-linked polymer electrolyte for lithium-sulfur batteries operating at subzero-temperatures. *Angew. Chem., Int. Ed.* **2024**, *63*, e202316087.

[212] Lu, H.; Su, Y. H.; Zhang, X. L.; Ma, Y. T.; Li, C.; Luo, S. L.; Kong, L.; Yuan, Y. Synergistic adsorption-diffusion-catalytic effect boosting polysulfides conversion by rational isotype heterojunction design for highly reversible lithium-sulfur batteries. *Adv. Funct. Mater.* **2025**, *35*, 2425863.

[213] Meng, W.; Wang, Y. D.; Zhou, X. C.; Chen, Z. J.; Zhao, Y.; Zhao, P. C.; Yuan, S.; Jin, Z.; Li, C. H. Azo-bridged metal-organic frameworks with robust Zr_6-cluster nodes: A dual-functional design for suppressing polysulfide shuttling in lithium-sulfur batteries. *J. Am. Chem. Soc.* **2025**, *147*, 44479–44491.

[214] Yang, J. L.; Xu, H. Y.; Xiao, T.; Li, J.; Yan, W. Q.; Zhang, T.; Fan, H. J. High-dimensional strain unlocks fast polysulfide redox kinetics for lithium-sulfur batteries. *Nat. Commun.* **2025**, *16*, 8910.

[215] Yu, S. X.; Zhang, C. Y.; Feng, J. N.; Shi, C.; Liu, Y.; Zhao, X. X.; Wang, T. Y.; Chen, S. Q.; Cheng, X. B.; Li, Q. et al. Synergistic electric-spin-dipole modulation for bidirectional polysulfide conversion toward reliable lithium-sulfur batteries. *Adv. Mater*., in press, DOI: 10.1002/adma.202510516.

[216] Zhao, Z. Q.; Pan, Y. K.; Yi, S.; Su, Z.; Chen, H. L.; Huang, Y. N.; Niu, B.; Long, D. H.; Zhang, Y. Y. Enhanced electron delocalization within coherent nano-heterocrystal ensembles for optimizing polysulfide conversion in high-energy-density Li–S batteries. *Adv. Mater.* **2024**, *36*, 2310052.

[217] Zheng, Q. Y.; Hou, Q.; Shu, Z. H.; Liu, G. Q.; Fan, X. X.; Wang, K.; Fan, J. M.; Yuan, R. M.; Zheng, M. S.; Dong, Q. F. An endogenous prompting mechanism for sulfur conversions via coupling with polysulfides in Li–S batteries. *Angew. Chem., Int. Ed.* **2023**, *62*, e202308726.

[218] Zhang, S. M.; Shi, H. D.; Tang, J. W.; Shi, W. X.; Wu, Z. S.; Wang, X. Super-aligned films of sub-1 nm Bi_2O_3-polyoxometalate nanowires as interlayers in lithium-sulfur batteries. *Sci. China Mater.* **2021**, *64*, 2949–2957.

[219] Yang, X. F.; Chen, Y. Q.; Wang, M. R.; Zhang, H. Z.; Li, X. F.; Zhang, H. M. Phase inversion: A universal method to create high-performance porous electrodes for nanoparticle-based energy storage devices. *Adv. Funct. Mater.* **2016**, *26*, 8427–8434.

[220] Huang, Y. Y.; Shen, M. H.; Yan, H. J.; He, Y. G.; Xu, J. Q.; Zhu, F.; Yang, X.; Ye, Y. X.; Ouyang, G. F. Achieving a solar-to-chemical efficiency of 3.6% in ambient conditions by inhibiting interlayer charges transport. *Nat. Commun.* **2024**, *15*, 5406.

[221] Li, W. N.; Li, X. J.; He, J. W.; Zhai, J.; Fan, X. Solar-enhanced blue energy conversion via photo-electric/thermal in GO/MoS_2/CNC nanofluidic membranes. *Small* **2025**, *21*, e06667.

[222] Liu, C. H.; Wang, Z. H.; Huang, Y. H.; Lu, Y. L.; Zheng, S. P.; Zhang, X. D.; Wu, K.; Chen, C. X.; Xu, H. S.; Pan, M. et al. Merging one- and multi-photon processes in hydrogen-bonded organic frameworks for enhanced NIR light-driven photothermal and photochemical conversions. *Angew. Chem., Int. Ed.* **2025**, *64*, e202511088.



Yiting Zhang is currently persuing a master's degree at Beihang University. Her current research interests focus on the cluster-induced controllable preparation of low-dimensional sub-1 nm materials and their applications in metal-air batteries.



Yu Zhang received his Ph.D. degree in Jilin University in 2007. Then he worked as a fellow in New Energy and Industrial Technology Development Organization, Hiroshima University, Japan. He joined Beihang University in 2013 and now is a full professor of the School of Chemistry. He focuses on Adv. Energy Mater., especially for optimizing electrode structures in Li-O_2 and Li/Na-ion battery field.



Junli Liu received her Ph.D. degree in Chemistry from Tsinghua University in 2020. Then she worked as a postdoctor at Tsinghu University from 2020 to 2022. In 2022, she became an associate professor in the School of Chemistry, Beihang University. Her current research focuses on the design and synthesis of cluster-induced low-dimensional sub-1 nm materials and their applications in battery energy storage.

Open Access This article is licensed under the terms of the Creative Commons Attribution 4.0 International License (http://creativecommons.org/licenses/by/4.0/), which permits use, sharing, distribution and reproduction in any medium, provided the original work is properly cited.

© The author(s) 2026. Published by Tsinghua University Press.